NTNU
Norwegian University of
Science and Technology

A Theoretic Study of ß'' Misfits and Strain in Al-Mg-Si Alloys

A Cluster-Based Approach Combining
Density Functional Theory and Linear
Elasticity

Sigurd Ofstad

Master of Science in Physics and Mathematics
Submission date: July 2018
Supervisor: Randi Holmestad, IFY

Norwegian University of Science and Technology
Department of Physics

Til mine foreldre, som tvang meg til å pugge gangetabellen.

Abstract

Heat treatable aluminium alloys of the 6xxx series are important for many industrial applications in the modern world. They contain small amounts of the alloying elements magnesium and silicon, which cluster together to form precipitate phases in the aluminium matrix. In particular, the metastable β″ precipitate strengthens the material significantly. This work calculates β″ misfits and surrounding strain fields in the host Al matrix by density functional theory. A cluster-based model is employed, with periodic boundary conditions along the precipitate habit direction, and a static boundary condition obtained by linear elasticity in the cross-sectional plane. A detailed account of modeling parameters and assumptions is made. Convergence of displacement related properties is assessed with respect to the modeling parameters. Simulations are performed on a range of realistically sized β″ precipitates, and atomic misfit values of the precipitates are calculated. The misfits, m_a and m_c, are larger by between 10%–30% relative to their experimentally reported counterparts, but fall below reported bulk values, as expected. m_a and m_c depend strongly on the precipitate aspect ratio, and decrease in response to an increased size in their respective lattice directions, consistent with previous experimental and theoretical reports. The misfit area decreases with precipitate size and is between 8.76%–9.75%, overestimating slightly compared to previously published results. Elastic strain around the precipitates is calculated and shown to be in good agreement with a previous pure DFT study of β″ in an Al lattice.

Sammendrag

Utherbare aluminiumlegeringer av 6xxx-serien er viktige for et vidt spektrum av anvendelser i den moderne verden. Disse legeringene inneholder en liten tilsats av legeringselementene magnesium og silisium, som opphopes i metallet og danner utfellinger i aluminiumstrukturen. Disse partiklene gjør materialet sterkere. Av de ulike presiptatene er den metastabile fasen β'' mest interessant, da den gir størst hardhetsøkning. Denne masteroppgaven kombinerer kvantemekaniske beregninger av den elektroniske strukturen i β''-presipitatet og det omkringliggende aluminiumgitteret med lineær elastisitetsteori for å studere atomær forskyvning i atomgitteret nær partiklene. En modell hvor presipitatet og omkringliggende aluminium modelleres som en flat, atomær sylinder, blir brukt. Forskjellige modelleringsparametre diskuteres i detalj sammen med de underliggende antakelsene. Simuleringer blir utført på et utvalg tidligere rapporterte presipitatstørrelser, og atomær mistilpasning blir beregnet. Mistilpasningene m_a og m_c er mellom 10% og 30% større enn deres eksperimentelle motparter, men faller under rapporterte verdier i bulk β''. m_a og m_c avhenger tydelig av presipitatets tverrsnittlige sideforhold, og avtar med økende sidelengde i deres respektive atomære gitterretninger. Dette overenstemmer med med tidligere teoretiske og eksperimentelle funn. Mistilpasningsarealet avtar med presipitatstørrelse, og er mellom 8.76% og 9.75%, litt i overkant av tidligere rapporterte verdier. Elastisk tøyningsfelt rundt presipitatene blir utregnet, og er i godt samsvar med tidligere DFT-studie av β'' i et aluminiumsgitter.

Preface

This document is the concluding work of a 30 ECTS master's course marking the finalization of my 5 years degree in Master of Science in Physics and Mathematics at the Norwegian University of Science and Technology. The work was carried out in Tokyo, Japan and Trondheim, Norway during the spring semester and summer of 2018. The work is a continuation of a 15 ECTS specialization project completed in fall of 2017.

The theme of this work has been the investigation of the displacement field surrounding the metastable strengthening precipitate β'' which forms in Al-Mg-Si alloys. Simulations of the electronic structure were performed with The Vienna Ab Initio Simulation Package for quantum mechanical calculations within the framework of density functional theory. Using this tool was an error-prone process, and countless hours were spent debugging simulations when they crashed. The silver lining is that this process gave me a thorough introduction to Linux along the way. In addition to all the other work, many hours were spent programming python scripts for analysis of the results. Some example code has been included in the appendix. Source code and VASP input files are available upon request at sigurof@gmail.com.

This thesis is written under the SFI CASA lower scale program. The cluster model employed is based on work by PhD student Jonas Frafjord. I would like to express my gratitude to him and Dr. Jesper Friis for all their help during our meetings. In addition, I would like to thank my professor, Randi Holmestad, for keeping herself updated on my progress even while running from one meeting to the next. And for creating the opportunity for me to experience an internship in an aluminium company in Japan. Finally, I would like to thank Stephane Dumoulin, SINTEF, for finding the time in his busy schedule to perform simulations that I needed as input for my calculations.

Table of Contents

Abbreviations

DFT	=	Density Functional Theory
LET	=	Linear Elastic Theory
PBC	=	Periodic Boundary Condition(s)
VASP	=	Vienna Ab Initio Simulation Package
SSSS	=	Super Saturated Solid Solution
GP zone	=	Guinier-Preston zone
HAADF	=	High Angle Annular Dark-Field imaging
STEM	=	Scanning Transmission Electron Microscope
LDA	=	Local Density Approximation
GGA	=	Generalized Gradient Approach
PAW	=	Projector Augmented-Wave method
FEM	=	Finite Element Method
PBE	=	Perdew, Burke and Ernzerhof

Chapter 1

Introduction

Aluminium is one of the most abundant elements on the earth, making up approximately 8% of the crust. Due to a high reactivity, aluminium occurs mainly in strong interatomic bindings in silicates and aluminium oxides, and was unavailable for widespread human use throughout most of history [1]. Aluminium production has grown immensely following the invention of effective industrial processes for extraction of aluminium from bauxite at the end of the 19^{th} century [2]. With the increased demand for lightweight materials for automotive and aerospace industries, aluminium production has seen a large surge during the last decade as well.

Much of the success of aluminium can be attributed to the versatility of its different alloys. One industrially important group of alloys are the heat treatable aluminium alloys, which can be strengthened considerably relative to pure aluminium by the addition of small amounts of other elements. This work is concerned with the strengthening process in the heat treatable 6xxx series alloys, which make up a number of indispensable materials for engineering purposes. The 6xxx alloys combine corrosion resistance and good weldability with moderate strength, and represent excellent materials for use in automotive, airplane, shipbuilding and architectural areas of production [3]. They owe their strength to an added few percent of magnesium and silicon, which under favorable temperature conditions during heat treatment grow into interstitial phases in the aluminium matrix called *precipitates*. The precipitates strengthen the metal by providing resistance to deformation, and understanding this process is important for improving alloys and production processes.

It is currently an active effort by several joint research projects between Hydro,

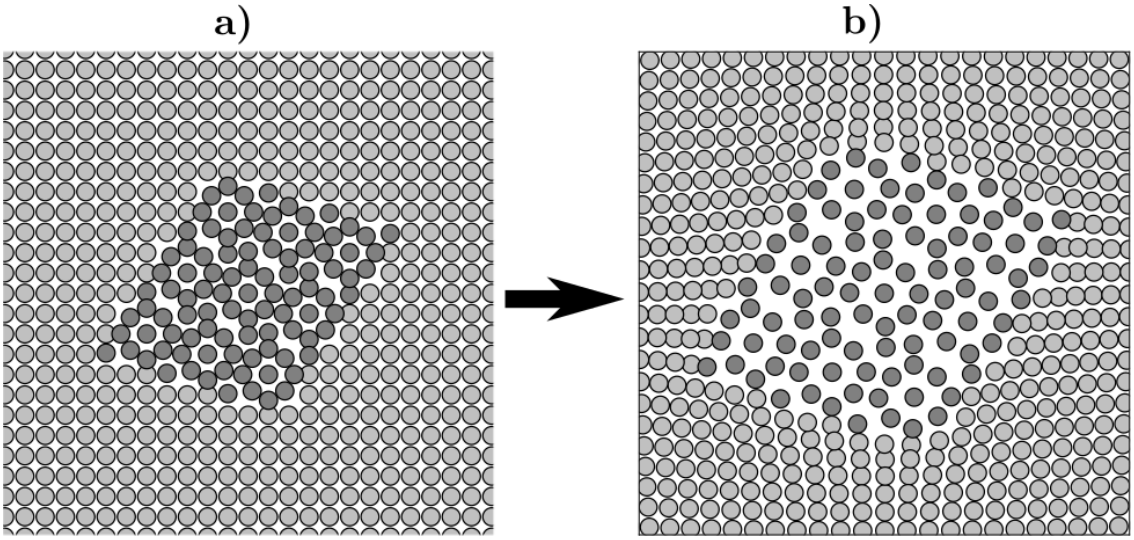

Figure 1.1: An illustration of a precipitate phase (in dark grey) occupying a portion of a surrounding host phase lattice (in silver). **a)**: A situation where the precipitate size matches the surrounding lattice perfectly. Hence, its atomic misfit is zero. Further, the surrounding lattice retains its perfect crystal structure, so the displacement field is zero. **b)**: A situation where the precipitate is larger than the portion of the surrounding lattice that it takes up, which means its misfit is positive and the precipitate generates a displacement field in the lattice.

SINTEF, NTNU and others to increase the knowledge of how macroscopic behavior in metals is affected by smaller scale processes. Having an accurate description of interactions on the atomic scale can provide more accurate parameters for use in macroscopic models.

Being a part of that effort, this work is concerned with the the atomic displacement field generated around β'' precipitates in the 6xxx aluminium alloys. These precipitates are slightly larger than the portion of the aluminium lattice that they occupy. This *misfit* causes the precipitate to push on the host lattice atoms, generating a *displacement field* radiating outwards into the host metal phase. Figure 1.1 illustrates an atomic displacement field generated by a large precipitate misfit. The displacement field gives the precipitates a region of influence larger than their actual physical size in the matrix. This may affect the behavior of solute elements and line defects near the precipitate, ultimately affecting precipitation mechanics. The authors of [4] show that interaction of the β'' precipitate displacement field with moving dislocations is likely a second order effect, meaning that its effect is subtle, but not negligible. Further, the displacement fields contribute a strain en-

ergy term to the total energy of precipitates, and are thus important for precipitate energetics, which have been used for assessing precipitate stoichiometry [5].

The precipitate misfit causes large perturbations of interatomic distances at the precipitate surface, necessitating an electronic level of accuracy to capture atomic behavior in this region. This should also pick up non-negligible contributions to the displacement field in the vicinity of the precipitate relative to a purely classical description. A few previous works have performed simulations on the displacement field around β'' with either hybrid [6] or full quantum mechanical levels of description [7, 8]. A recent experimental study [9] also studied the effects of atomic displacement around entire precipitates.

The present work introduces a model combining first principles quantum mechanical calculations with linear elastic calculations to determine the misfits and displacement fields of precipitates with varying dimensions. The quantum mechanical simulations are performed by electronic structure calculations within the framework of density functional theory (DFT), and linear elastic calculations are performed with the finite elements method (FEM). The results are compared with various previous works, focusing in particular on the experimental work mentioned.

The model is a cluster model, more commonly used in dislocation modeling [10]. The precipitate is assumed to be infinitely long, with no misfit along the [0 0 1] direction of the aluminium lattice. Thus, it is enough to simulate a one unit cell thick cross-sectional slab of atoms. The atomic slab is divided into an inner cylinder, containing the precipitate, surrounded by an annulus region. Refer to Figure 3.1 for a schematic illustration of the model. The atomic positions in the inner cylinder are optimized to their structural ground state, while the outer annulus atoms are kept static in positions given by LET. Because the DFT code employed uses periodic boundary conditions, an isolating vacuum is included around the atomic slab in the cross-sectional plane to mitigate mutual interaction across the boundary. It is hypothesized that this model could yield more accurate results for atomic displacement than the somewhat similar model used the works by Ninive et al. [7, 8, 11]. Those studies used a model where the precipitates lie in an aluminium lattice directly connected to its periodic repetitions. This is equivalent to a physical situation with an infinite number of mutually parallel, densely packed precipitates. It is suspected this could lead to some degree of underestimation of the displacement field at the boundaries of the simulation cell used, as the precipitate displacement fields

push against each other. This effect is not present in the current model, because the atomic displacement in the static region is supposed to be qualitatively correct, forcing the inner region to obtain a solution relatively close to the real situation.

This thesis is divided into the following chapters, introduction, theory, modeling and methodology, results and discussion and concluding remarks. The theory chapter contains a brief introduction to the fundamental concepts, covering alloys, precipitates, linear elasticity and the fundamentals of density functional theory. The modeling and methodology chapter begins with a motivation part, followed by a detailed account of the proposed model, then a discussion of assumptions and important parameters, and ends with a concise account of the methodology. The results and discussion chapter compares the results with previous studies. Last in the main text is the conclusion chapter. A list of acronyms has been included for convenience above the current chapter. The main text is followed by an appendix with an example of some of the input files used for DFT calculations.

Chapter 2

Theory

This chapter provides an introduction to alloys and age hardening before going into details about the 6xxx alloy system and the β'' precipitate. A brief explanation of linear elasticity follows, before outlining the fundamentals of density functional theory (DFT). The chapter ends with a review of important numerical aspects of plane-wave DFT calculations.

2.1 Alloys and Precipitate Hardening

An alloy is a compound mixture of a metallic phase with one or several additional elements. For example, brass is usually 55% to 90% copper and the rest is mainly zinc [12]. Steel consists of iron with up to 2% carbon [13], and aluminium foil contains close to 99.4% aluminium, the rest being Si and Fe [14]. It is not always the case that the additional elements mix evenly with the main element — they may cluster together and form secondary phases called *precipitates*. The main phase surrounding it is then referred to as the host phase. Another term, host matrix, is an expression which means the host phase with emphasis on its regular crystal structure on the atomic level.

Alloys are very important to modern industries because of their often superior material properties over pure metals. For example, if the pure form of some metal was soft, adding some additional elements could render a strong alloy but reduce its corrosion resistance and ductility. Because improving one property could deteriorate another, the production of alloys is often about finding good compromises between different material properties. Aluminium is a quite soft metal which can achieve a

very high strengthening factor through alloying with other elements. Aluminium alloys obtain their properties through a variety of industrial processes including casting, extrusion, annealing, work hardening and age hardening. Of those, age hardening is the most important for this work.

Age hardening increases the yield strength of an alloy and is performed last in a sequence of quenching and heating in different conditions depending on the desired alloy properties. First, to make a homogeneous structure, the alloy is heated to temperatures in the vicinity of 530 °C [15]. The speed of atomic diffusion increases exponentially with temperature [16], so the elements begin to distribute uniformly throughout the solid. This process is called solution heat treatment and forms what is referred to as a solid solution. The alloy is subsequently put through rapid cooling, usually by quenching in water, to prevent formation of the equilibrium precipitate during the cooling process [17]. The quenching of the alloy slows down the rate of thermal diffusion and traps the atoms in a state where the diffusion energy barrier is much greater than the thermal energy of each atom. Normally it would be more stable for the alloying constituents to rearrange and precipitate but there is no driving force for that at low temperatures. This state can be imagined as a local energy minimum in the configurational space of the alloy atoms and in this state it is referred to as a super-saturated solid solution (SSSS). The procedure is followed by room temperature aging or artificial aging at temperatures around 160 °C–180 °C [15, 17]. During the interval of aging, the alloy strength increases as the alloying elements rearrange due to thermally activated diffusion. Different temperatures and storing times can be used to control the final condition of the product.

The hardening effect is caused by the formation of precipitates, which are small particles inside the host phase that slow down deformation of the metal. Plastic deformation of metals occur by the formation and movement of dislocations. The simplest type of dislocations is the edge dislocation, which can be imagined as the presence of an extra half-plane of atoms in the periodic lattice. Figure 2.1 is a cross-sectional view of an edge dislocation. The dislocation line follows the border of the extra atomic plane into the page. Precipitates act as obstacles to the propagation of line defects such as edge dislocations in the matrix. One of the ways that a propagating dislocation can pass a precipitate is by shearing it. Precipitates require a larger shear stress than the host lattice for the dislocation to pass through,

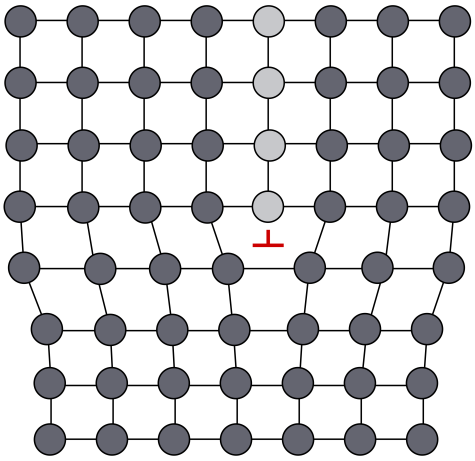

Figure 2.1: A cross-sectional view of an edge dislocation in a regular lattice. The extra half-plane of atoms is indicated in silver grey, and the dislocation line, indicated in red, follows the edge of that plane, extending into the page.

and hence obstruct the movement of the dislocation.

Precipitates form as a way for the system to reduce its Gibbs energy, and different precipitates will dominate the host lattice at different elapsed times of the age hardening process. The equilibrium precipitate can be preceded by several metastable precipitate phases due to an energy barrier in its formation. The intermediate phases have a smaller barrier, and thus form more easily at lower temperatures.

Precipitates often grow as needle or plate-like structures in the host phase in certain crystallographic directions or planes, which are termed habit directions and habit planes. The relation between the crystallographic directions in different phases (such as precipitate and matrix) is commonly expressed in the following manner,

$$\begin{aligned} &\textbf{Planes} && (h\,k\,l)_{\beta} \parallel (u\,v\,w)_{\alpha} \\ &\textbf{Directions} && [h\,k\,l]_{\beta} \parallel [u\,v\,w]_{\alpha}, \end{aligned}$$

where the variables h, k, l and u, v, w are integers. This notation indicates that the planes $(h\,k\,l)$ and directions $[h\,k\,l]$ in some phase β are parallel to the planes $(u\,v\,w)$ or the directions $[u\,v\,w]$ in the phase α, respectively.

In some alloys the crystal lattice extends almost continuously across the matrix-

precipitate interface causing a strain field which radiates outwards in the host matrix. Being close to coherent, one calls this sort of interface semi-coherent. At a semi-coherent interface, the lattice of the host phase is mainly preserved except for a slight periodic misfit when crossing into the precipitate phase. The periodic misfit is owed to the precipitate having different elastic constants than the host lattice, meaning it will be slightly larger or smaller than the aluminium atoms it has replaced. For large particles this disregistry builds up and is periodically alleviated by misfit dislocations.

The strain field surrounding semi-coherent precipitates will interact with moving dislocations and solute elements, indirectly influencing their movement. One precipitate well known for generating surrounding strain fields is the β'' precipitate in age-hardenable aluminium alloys. The next section will outline important aspects of aluminium and this precipitate.

2.2 Al-Mg-Si Alloys and β''

This work is a case study of the most important hardening precipitate of the aluminium 6xxx alloy series, β'' [18]. The designation of 6xxx stems from the aluminium alloy designation system, which classifies wrought aluminium alloys by four digits from 1xxx to 8xxx [15]. The first digit symbolizes the main alloying element(s), which in the case of the 6xxx alloys are magnesium and silicon. Therefore, the 6xxx alloys are often referred to as Al-Mg-Si alloys. The introduction chapter touched on the various uses and merits of Al-Mg-Si alloys, and this section will introduce the atomistic details of the system.

The precipitation sequence in Al-Mg-Si alloys during aging is generally accepted to be SSSS $\rightarrow$ Mg/Si clusters $\rightarrow$ Guinier-Preston (GP) Zones $\rightarrow \beta'' \rightarrow \beta'$, U2, U1, B$' \rightarrow \beta$ [19]. Here, SSSS is the super-saturated solid solution after quenching of the alloy in the age hardening process. The precipitates called GP zones are named after Guinier and Preston, who first studied these precipitates. They are common for many alloy precipitate systems, and are usually fully or semi-coherent with the host matrix. Andersen et al. [20] report the GP zones in Al-Mg-Si to be fully coherent with the host matrix, and that peak hardness occurs when a combination of GP zones and β'' dominates the Al matrix. U2, U1 and β'' form as long rods in the host matrix around pillar-like columns of silicon which form early in the pre-

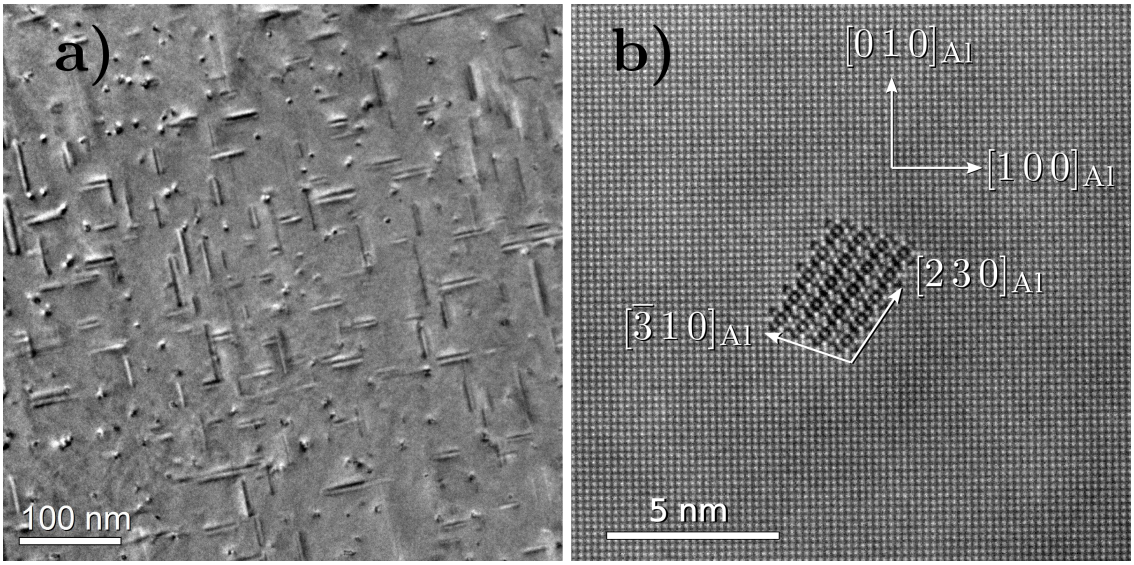

Figure 2.2: **a)** β″ needle structure as seen by a transmission electron microscope. It can be seen how some rods are pointing out of the image plane, appearing as scattered blobs. The image is reproduced with permission from Dr. Calin D. Marioara, SINTEF. **b)** A cross-sectional view of a β″ precipitate in the aluminium matrix taken by aberration-corrected high-resolution scanning transmission electron microscopy. The needle direction points out of the image plane. The image is reproduced with permission from Dr. Sigurd Wenner, SINTEF.

cipitation sequence [21]. β″ habits the $\langle 0\,0\,1\rangle$ directions of the aluminium matrix and the length is typically around 300-1500 Å, with a thickness of approximately 30 Å in the peak hardness tempering condition [9, 20]. Refer to Figure 2.2 **a)** for a view of β″ lying in the $\langle 0\,0\,1\rangle_{\mathrm{Al}}$ directions and **b)** for a cross-sectional view of β″. The length ratio R_{L}, defined further down, of the cross-sectional lengths differs significantly from one needle to the other, and has been reported between 0.77 and 3.25 [9].

Aluminium belongs to space group 225, with the face-centered cubic structure. Its lattice parameter is the same along the basis vectors of its unit cell and measures $a_0 = 4.03\,\text{Å}$ at 0 K [22] and $a_0 = 4.05\,\text{Å}$ at room temperature [23]. Figure 2.3 shows the FCC structure with the lattice vectors along the x, y and z axes of the cartesian coordinate system. The present work takes the lattice vectors of aluminium to be $\boldsymbol{a}_{\mathrm{Al}} = a\hat{\boldsymbol{x}}$, $\boldsymbol{b}_{\mathrm{Al}} = a\hat{\boldsymbol{y}}$ and $\boldsymbol{c}_{\mathrm{Al}} = a\hat{\boldsymbol{z}}$, where a is the value of the aluminium lattice parameter, and $\hat{\boldsymbol{x}}$, $\hat{\boldsymbol{y}}$ and $\hat{\boldsymbol{z}}$ are the unit vectors along the cardinal directions of the cartesian coordinate system.

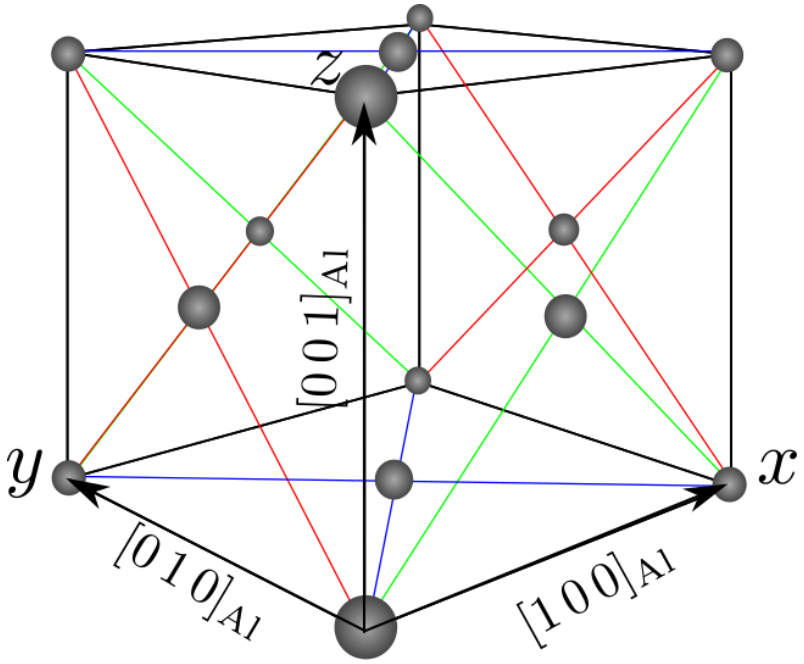

Figure 2.3: The face-centered cubic (FCC) structure seen here is a cubic cell with an extra lattice point at the center of each face. The diagonal line elements indicate the planes of the cubic unit cell. This figure shows 14 atoms, but they are shared with other unit cells and only a total of four whole atoms reside within each.

β″ is monoclinic and belongs to the space group C2/m [20]. The vector relations of its unit cell with the aluminium lattice are

$$\begin{aligned} \boldsymbol{a}_{\beta''} &= (1+m_{\boldsymbol{a}})(2\boldsymbol{a}_{\mathrm{Al}} + 3\boldsymbol{b}_{\mathrm{Al}}), \\ \boldsymbol{b}_{\beta''} &= (1+m_{\boldsymbol{b}})\boldsymbol{c}_{\mathrm{Al}}, \\ \boldsymbol{c}_{\beta''} &= (1+m_{\boldsymbol{c}})\tfrac{1}{2}(-3\boldsymbol{a}_{\mathrm{Al}} + \boldsymbol{b}_{\mathrm{Al}}), \end{aligned} \tag{2.1}$$

where m_a, m_b and m_c are misfit fractions, indicating that the β″ unit cell is slightly larger than the region of aluminium atoms it replaces. The lattice directions $\boldsymbol{a}_{\beta''}$ and $\boldsymbol{c}_{\beta''}$ in Equation 2.1 are indicated in Figure 2.2 **b)**. $\boldsymbol{b}_{\beta''}$ points out of the image plane. A recent study reported the misfits m_a and m_c to lie between 1.61%-3.66% and 2.53%-7.26%, respectively for varying precipitate dimensions [9]. The β″ precipitate has a semi-coherent interface with the host matrix, and the misfits cause it to displace the aluminium lattice at its interface. This generates a displacement field around β″, as was illustrated in Figure 1.1. The misfit m_b is known to be very small and is usually assumed to be negligible. For the purpose of this work it will be set to zero.

The most likely formula unit for β″ has been a topic of discussion for many

years, early reports suggesting Mg_5Si_6 [20, 21], with later research indicating that the precipitates have a 20 atomic percentage of aluminium [5]. Calculations by ab initio methods indicate that $Al_2Mg_5Si_4$ is the most energetically stable composition [8], supported by very recent results by dispersive X-ray spectroscopy [24]. However, some results by HAADF-STEM seem to indicate $Al_3Mg_4Si_4$ [8]. It is possible that the unit cell of β″ can exist with varying compositions, and the effect of temperature may play an important role in the formation energies as in the θ' precipitate of the Al-Cu alloy system [25]. Regardless, such a treatment is beyond the scope of the current work, which will assume β″ has the composition $Al_2Mg_5Si_4$.

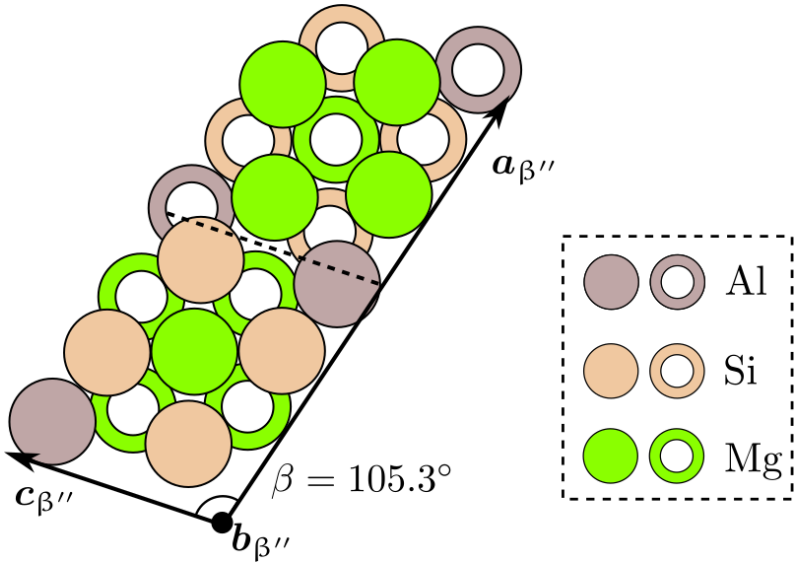

Figure 2.4: A vertical projection of the β″ unit cell assuming the composition $Al_2Mg_5Si_4$. The stippled line separates the two antisymmetric formula units. The experimental cell parameters in the cross-sectional plane are shown. The lattice vector $\boldsymbol{b}_{\beta''}$ points out of the plane. The atoms lie in two planes separated by half the unit cell parameter in the $\boldsymbol{b}_{\beta''}$ direction. The filled spheres lie in the upper plane and the hollow spheres lie in the lower plane.

The β″ unit cell is illustrated in Figure 2.4. Breaking somewhat with convention from other works [6, 8, 19, 26, 27], the unit cell is drawn so that the reader can easily identify the unit cell as consisting of two equal formula units on each side of the unit cell. A formula unit consists of four Mg atoms at approximately mutually right angles relative to a central Mg atom and four Si atoms at 45° angles to the Mg atoms. There are two Al atoms on opposite sides of the cluster. It is common for β″ to appear in half-integer unit cells in the $\boldsymbol{a}_{\beta''}$ lattice direction. To avoid

using half-integer unit cells, the present work will use the terms 'eye' or formula unit meaning a half unit cell consisting of a single formula unit $Al_2Mg_5Si_4$ in the spatial arrangement illustrated in Figure 2.4. Further, n_a and n_c will be taken to mean the number of eyes in each of the lattice directions. This way, an $n_a \times n_c$ precipitate will be taken to mean a quadrilateral precipitate of dimensions $\frac{1}{2}n_a\boldsymbol{a}_{\beta''}$ by $n_c\boldsymbol{c}_{\beta''}$.

In the discussion of misfits, the length ratio is defined as the ratio between the relaxed β'' precipitate side lengths,

$$R_{\mathrm{L}} = (n_a a_{\beta''})/(2n_c c_{\beta''}). \tag{2.2}$$

On the other hand, the *aspect ratio* will be taken to be taken as the simple fraction between the number of eyes, n_a/n_c. The aspect ratio will generally be relatively close to R_{L} because a single formula unit is almost the same length in both cross-sectional lattice directions.

2.3 Linear Elasticity

Linear elasticity is a branch within continuum mechanics which fundamentally assumes deformations of a material to be infinitesimal. Deformations can be measured by the quantity strain, which quantifies tension/compression of the material and is symbolized by ϵ. Strains are assumed to induce linearly related forces in the material, called stress, symbolized by σ. The strain-stress relation is a generalization of the one-dimensional Hook's law to three dimensions, and is expressed as [28]

$$\sigma_{ij} = C_{ijkl}\epsilon_{kl}, \tag{2.3}$$

where C_{ijkl} is the stiffness tensor corresponding to the spring constant in the one-dimensional Hook's law.

In principle the stiffness tensor has 81 elements, but symmetry constraints and energy arguments reduce the total number to 21 independent components. Further reduction is possible given certain conditions depending on the nature of the material in question. The linear elastic simulations in the present work assume orthotropic elasticity, in which the material lattice vectors are mutually orthogonal. In this case, only nine independent components of the stiffness tensor remain.

2.3.1 Strain

As mentioned, strain is a measure of the deformation of a material and is defined as the derivative of a continuous displacement field. For the atomic models calculated in this work, the displacement field is only defined at lattice points and the usual definition of strain is not immediately applicable. Therefore, a reformulation of the strain is needed. The strain matrix in two dimensions is

$$\epsilon_{ij} = \frac{1}{2}(e_{ij} + e_{ji}), \tag{2.4}$$

where, e_{ij} is the extension, defined as the derivative of the displacement field $\boldsymbol{u}(x_0, x_1) = \sum_{i=1}^{2} u_i \hat{\boldsymbol{x}}_i$,

$$e_{ij} = \frac{\partial u_i}{\partial x_j}, \tag{2.5}$$

and $x_0 = x$, $x_1 = y$ are the coordinates in the two-dimensional plane.

In the present work, e_{ij} is defined by a central difference scheme as the difference in displacement in the x_i direction between equal lattice sites in adjoining unit cells along the x_j direction in the strained state, Δu_{ij}, relative to the unstrained lattice parameter a_j,

$$e_{ij} = \frac{\Delta u_{ij}(m, n)}{a_j}. \tag{2.6}$$

This equation is combined with Equation 2.4 to calculate the strains. The notation $0 \to x$, $1 \to y$ will be used for the subscripts, so $\epsilon_{xx} = \epsilon_{00}$ and $\epsilon_{yy} = \epsilon_{11}$. Note that a_j, does not depend on j because the lattice constant is isotropic along the primitive lattice vectors of the FCC structure. The extension e_{ij} is assigned to the lattice point in the middle of the two lattice points used for its calculation. This has the advantage of yielding a symmetric strain field around the precipitate and is intuitively understandable as it assigns the shared compression between two lattice sites to a point equally far between them both. On the precipitate interface, some aluminium lattice points do not have neighboring lattice points inside the precipitate, because they are replaced by Si and Mg. Hence, a central derivative definition of Δu_{ij} cannot be calculated. Instead, a forward or backward derivative is used for those lattice points, depending on which lattice point is missing.

2.4 Density Functional Theory

To study the electronic structure of materials, it is often of central importance to solve the time-independent Schrödinger equation for an isolated system of interact-

ing particles. With Ψ as the all-particles wave function, the Schrödinger equation reads

$$\hat{H}\Psi = E\Psi, \tag{2.7}$$

where $\hat{H}$ is the Hamiltonian operator and E is the total energy of the system. $\hat{H}$ and Ψ depend on all particle positions. The Hamiltonian operator can be divided into

$$\hat{H} = \hat{T}_\mathrm{n} + \hat{T}_\mathrm{e} + \hat{V}_\mathrm{nn} + \hat{V}_\mathrm{ee} + \hat{V}_\mathrm{ne}, \tag{2.8}$$

where $\hat{T}_\mathrm{n}$ and $\hat{T}_\mathrm{e}$ are the total nucleus and electron kinetic energy operators respectively. $\hat{V}_\mathrm{nn}$, $\hat{V}_\mathrm{ne}$ and $\hat{V}_\mathrm{ee}$ are the nucleus-nucleus, nucleus-electron, and electron-electron total potential energy operators. The total energy E has corresponding contributions for each of the above operators, which will be denoted by the same symbol without the hat.

2.4.1 The Born-Oppenheimer Approximation

The electron is almost two thousand times less massive than the proton and the neutron. For a given distribution of nuclei and electrons, the latter will find the most energetically favored configuration almost instantaneously. This means that in any instant, for a system with M nuclei and N electrons, one can assume the positions of the nuclei, $\boldsymbol{R}^M = (\boldsymbol{R}_1, \boldsymbol{R}_2, \ldots, \boldsymbol{R}_M)$, to be fixed. This allows one to separate out from the total wave function Ψ an electronic wave function $\Psi_\mathrm{e} = \Psi_\mathrm{e}(\boldsymbol{r}^N)\big|_{\boldsymbol{R}^M \text{fixed}}$, depending only on the electron positions, $\boldsymbol{r}^N = (\boldsymbol{r}_1, \boldsymbol{r}_2, \ldots, \boldsymbol{r}_N)$. This is called the Born-Oppenheimer approximation and enables the use of a separate electronic Schrödinger equation, defined as

$$\hat{H}_\mathrm{e}\Psi_\mathrm{e} = E_\mathrm{e}\Psi_\mathrm{e}. \tag{2.9}$$

The electronic energy E_e is determined by the electronic Hamiltonian

$$\hat{H}_\mathrm{e} = \hat{T}_\mathrm{e} + \hat{V}_\mathrm{ee} + \hat{V}_\mathrm{ne}. \tag{2.10}$$

It is of interest to take a closer look at the last term. It can be defined as

$$\hat{V}_\mathrm{ne} = \sum_{i=0}^{N} v(\boldsymbol{r}_\mathrm{i}), \tag{2.11}$$

where $v(\boldsymbol{r})$ is the total potential of the M nuclei that the electrons see at position $\boldsymbol{r}$, and is referred to as the *external potential*.

2.4.2 The Hohenberg-Kohn Theorems

Hohenberg-Kohn [29] introduced two theorems which greatly simplify analysis of the above defined problem of N interacting electrons in the Born-Oppenheimer approximation.

1. The first theorem states that, up to a trivial added constant, there is a one-to-one relation between the external potential, $v(\boldsymbol{r})$, and the ground state electron density,

$$\rho(\boldsymbol{r}_1) = N \int |\Psi_\mathrm{e}(\boldsymbol{r}_1, \boldsymbol{r}_2, \ldots, \boldsymbol{r}_N)|^2 \, \mathrm{d}\boldsymbol{r}_2 \ldots \mathrm{d}\boldsymbol{r}_N, \tag{2.12}$$

   which gives the statistical expectation value of the number of electrons in an infinitesimal volume d^3r to be $\rho(\boldsymbol{r}_1)\,\mathrm{d}^3r$. Thus, there is one unique electron density to every possible external potential, which again uniquely determines $\hat{H}_\mathrm{e}$. This means that it is possible to write the electronic energy of Equation 2.9 as a functional of ρ,

$$E_\mathrm{e}[\rho] = V_\mathrm{ne}[\rho] + F[\rho], \tag{2.13}$$

   where $F[\rho] = T_\mathrm{e}[\rho] + V_\mathrm{ee}[\rho]$ contains the kinetic and potential energies from the electrons only.

2. The second theorem states that the electron density $\rho(\boldsymbol{r})$ which minimizes the energy functional of 2.13 corresponds to the ground state electronic wave function Ψ_e. It is therefore equal to the ground state electron density ρ_0. Hence, it is possible to search for the ground state of the electronic wave function by applying the variational method to equation 2.13.

Together, the Hohenberg-Kohn theorems reduce the dimensionality of the electronic structure problem. Minimizing the energy of Ψ_e has gone from being a minimization problem in $3N$ dimensions to a problem in 3 dimensions. Note that any theory which uses a density as the basic variable is called a *density functional theory* (DFT). However, the term is often used synonymously with quantum mechanical electronic structure calculations because the latter often employs the framework of DFT.

2.4.3 The Kohn-Sham Equations

The Hohenberg-Kohn theorems now dictate that E_0 is the minimum value of the electronic energy functional 2.13 with respect to ρ. To find this minimal value, one applies the variational principle by finding the functional derivative of Equation 2.13 while applying the constraint

$$\int \rho(\boldsymbol{r})\,\mathrm{d}\boldsymbol{r} = N, \tag{2.14}$$

which is equivalent to imposing normalization upon the total electronic wave function. The resulting equation can be rearranged to describe a system of noninteracting electrons in a redefined, corresponding, external potential which includes the electron-electron interactions. As it happens, the wave function of a system of noninteracting electrons is well known to take the form of a so-called *Slater determinant*

$$\Psi_\mathrm{s} = \frac{1}{\sqrt{N!}} \det \begin{pmatrix} \psi_1(\boldsymbol{r}_1) & \psi_2(\boldsymbol{r}_1) & \cdots & \psi_N(\boldsymbol{r}_1) \\ \psi_1(\boldsymbol{r}_2) & \psi_2(\boldsymbol{r}_2) & \cdots & \psi_N(\boldsymbol{r}_2) \\ \vdots & \vdots & \ddots & \vdots \\ \psi_1(\boldsymbol{r}_N) & \psi_2(\boldsymbol{r}_N) & \cdots & \psi_N(\boldsymbol{r}_N) \end{pmatrix} \tag{2.15}$$

exactly. ψ_i are the N lowest eigenstates of the single-electron Schrödinger equation

$$\left[-\frac{1}{2}\boldsymbol{\nabla}^2 + v_\mathrm{s}\right]\psi_i = \epsilon_i \psi_i, \tag{2.16}$$

where $i = 1 \ldots N$ and $\boldsymbol{\nabla}$ is the nabla operator in three dimensions. v_s is the effective potential, which contains the contributions from the external potential and the electron-electron interactions. It can be seen that the determinant overhead is antisymmetric with respect to the interchange of two electrons, and so automatically fulfills the Pauli exclusion principle. The total electronic energy is

$$E[\rho] = \sum_{i=1}^{N} \epsilon_i, \tag{2.17}$$

which is the sum of the single electron energies. Equations 2.16 and the expression for v_s are together known as the *Kohn-Sham equations* and solve exactly the problem of N interacting electrons. The detailed expression for v_s is not so relevant for the present discussion but suffice it to say that one of its terms is called the exchange-correlation potential, $V_\mathrm{xc}[\rho]$, and, in contrast to the other terms, has been impossible to calculate a precise analytical expression for. Hence, the exact dependence of the

exchange-correlation potential V_{xc} on ρ is unknown, and must be approximated to be able to solve the KS equations. Two of the famous approximations to the exchange-correlation potential are the *local density approximation* (LDA) and the *generalized gradient approach* (GGA). The former is known for its simplicity which renders surprisingly accurate results, despite a simplistic treatment of the problem. The latter method is the result of a more accurate treatment of the exchange-correlation potential and provides very accurate energies for most applications.

2.4.4 The Self-Consistent Approach

Notice that Equations 2.16 yield the orbitals ψ_i, from which ρ is given. However v_{s} depends on ρ, so to solve the equation one needs ρ. The equation can be solved by beginning with an initial guess for the electron density, ρ_{trial}. Solving the equations for ρ, one gets a new trial function. The procedure is applied iteratively until consecutive solutions reach *self-consistency*. This could be e.g. when the difference between consecutive values of the total electronic energy in 2.17 reaches some threshold value.

2.5 Numerical Aspects of DFT

In the present work all electronic structure calculations have been made using the commercial Vienna Ab initio Simulation Package (VASP). Borrowing from the home page of VASP [30], "The Vienna Ab initio Simulation Package (VASP) is a computer program for atomic scale materials modelling, e.g. electronic structure calculations and quantum-mechanical molecular dynamics, from first principles." First principles or ab initio calculations are entirely void of empirical laws and instead based on physical theoretical background only. The following section will cover important aspects of electronic structure calculations which have been instrumental to their success as a commonly applied tool for analysis.

The following sections attempt to outline a few important aspects of the single-electron orbitals in real simulations. Prioritizing brevity over accuracy, the discussion has been simplified significantly.

2.5.1 Representation of the Single-Electron Orbitals

VASP enforces periodic boundary conditions on the system in question and for this reason most properties are represented by plane-wave expansions. The periodic boundary conditions are defined by three supercell lattice vectors $\boldsymbol{a}_{\mathrm{sc}}$, $\boldsymbol{b}_{\mathrm{sc}}$ and $\boldsymbol{c}_{\mathrm{sc}}$. The supercell is then the parallelepiped spanned by those vectors. Within this paradigm the effective potential v_{s} is periodic with respect to any translation of the form $\boldsymbol{T} = n_a\boldsymbol{a}_{\mathrm{sc}} + n_b\boldsymbol{b}_{\mathrm{sc}} + n_c\boldsymbol{c}_{\mathrm{sc}}$, where n_a, n_b and n_c are integers. Then the Bloch theorem states that the solutions of the wave function should be plane waves modulated by a periodic function,

$$\psi_{n\boldsymbol{k}}(\boldsymbol{r}) = u_{n\boldsymbol{k}}(\boldsymbol{r})e^{i\boldsymbol{k}\cdot\boldsymbol{r}}, \tag{2.18}$$

where $u_{n\boldsymbol{k}}(\boldsymbol{r})$ has same periodicity in $\boldsymbol{T}$. For computational reasons it is desireable to represent $u_{n\boldsymbol{k}}$ and other periodic quantities in plane-waves by a Fourier expansion:

$$u_{n\boldsymbol{k}}(\boldsymbol{r}) = \sum_{\boldsymbol{G}} C_{\boldsymbol{G}n\boldsymbol{k}}e^{i\boldsymbol{G}\cdot\boldsymbol{r}}, \tag{2.19}$$

where $\boldsymbol{G}$ are the reciprocal lattice vectors of the supercell lattice. Courtesy of the Fourier expansion, the total energy and the Hamiltonian are easy to implement.

2.5.2 The Frozen Core and PAW Method

Because of the mutual orthogonality required of wave functions, they exhibit large oscillations near the core and representing them requires many terms in the plane-wave expansion. Bonding is determined largely by the valence electrons, whereas the core electron states are strongly localized and vary only insignificantly during calculations. For this reason one assumes those to be unchanging during most simulations and calculate them in a separate run. Due to the frozen nature of the core electron states it is called the *frozen core approximation*.

Another important simplifying procedure is related to the valence electrons. Because of the orthonormality requirements with the core electron states, they experience rapid oscillations near the atomic core. This is expensive in the plane-wave representation. The projector augmented-wave (PAW) method alleviates this issue by representing the wave functions by pseudo wave functions which are more well behaved close to the core. The method requires a reevaluation of the single-electron wave functions, energies and operators but these considerations are too

lengthy for the current discussion.

2.5.3 Cut-off Energy

Usually the number of harmonic terms needed to express $u_{n\boldsymbol{k}}(\boldsymbol{r})$ is infinite. For any continuous function the coefficients $C_{\boldsymbol{G}n\boldsymbol{k}}$ must approach zero for high enough values of $\boldsymbol{G}$, which means it is sufficient to sum over a finite number of terms. A value of the kinetic energy is used to define the highest included mode of the plane wave expansion, and is called the *cut-off energy*,

$$E_{\text{cutoff}} > \frac{1}{2}|\boldsymbol{G} + \boldsymbol{k}|^2, \tag{2.20}$$

and all contributions from harmonics of higher energy than E_{cutoff} are left out.
E_{cutoff} must be chosen carefully. It can significantly alter the accuracy of the simulation if set too low. It should be as low as feasible while introducing only insignificant errors. If one runs the same simulation consecutively while increasing the cut-off energy, one will observe that the total energy changes significantly from one to the next in some interval and then becomes almost constant between simulations. The interval of most change is where the most energetic energy contributions are located. When exceeding some value, the harmonic coefficients are close to zero. In this area, the electronic energy is said to be converged with respect to the cut-off energy. The process of determining sufficient values for various parameters in this manner is called *convergence testing*.

2.5.4 k-point Sampling

Various important quantities are evaluated by numerical integration of some property over the first Brillouin zone of the reciprocal space of the lattice supercells. In general one may write

$$A = \int_{\text{BZ}} a(\boldsymbol{k})\,\mathrm{d}\boldsymbol{k}, \tag{2.21}$$

where one is interested in the value of A and $a(\boldsymbol{k})$ must be integrated. $\boldsymbol{k}$ is the lattice vector in supercell reciprocal space. To approximate the integral one uses an equally spaced mesh of points in reciprocal space. Due to symmetry certain points have the same value, and the integral can be approximated by a weighted sum over the reduced set of points, the k-points k_i,

$$A \approx \tilde{A} = \sum_i w_{\boldsymbol{k}_i} a(\boldsymbol{k}_i)\Delta\boldsymbol{k}_i, \tag{2.22}$$

where $w_{\boldsymbol{k}_i}$ denotes a set of weights and $\mathrm{d}\boldsymbol{k} \to \Delta\boldsymbol{k}$. Often the grid of k-points $\boldsymbol{k}_i$ is chosen so that the k-point density is the same in the three reciprocal directions. Further, the grid may include the origin of the Brillouin zone, called the gamma point, or not. The former option is usually safer because it preserves the symmetry used for reducing the necessary number of k-points [31].

As with E_{cutoff}, the distribution of k-points in reciprocal space is very important for the accuracy of results. One should perform convergence tests of the total energy with respect to the k-point density to determine a sufficient value.

2.5.5 Smearing of the Fermi-Surface

In metals, integrals involving the occupancy of states present a numerical problem due to very slow convergence with respect to the number of k-points. This is solved by introducing partial occupancies of electronic states. For example, one needs to calculate the energy per supercell, given by

$$\sum_n \frac{1}{\Omega_{\mathrm{BZ}}} \int_{\mathrm{BZ}} \epsilon_{n\boldsymbol{k}} f_n(\boldsymbol{k})\, \mathrm{d}\boldsymbol{k}, \tag{2.23}$$

where Ω_{BZ} is the volume of the first Brillouin zone, and $\epsilon_{n\boldsymbol{k}}$ is the energy of an electronic state. $f_n(\boldsymbol{k})$ is the occupancy level of the electronic states. In metals at 0 K, $f_n(\boldsymbol{k})$ is described by the step function $\Theta(\epsilon_{n\boldsymbol{k}} - \mu)$ where μ is the Fermi level. Thus, the occupancy level drops from one to zero across the Fermi surface in $\boldsymbol{k}$ space. Following the discussion on sampling of k-points, Equation 2.23 takes the following form,

$$\sum_{\mathrm{n}} \sum_{\boldsymbol{k}} w_{n\boldsymbol{k}} \epsilon_{n\boldsymbol{k}} \Theta(\epsilon_{n\boldsymbol{k}} - \mu) \Delta\boldsymbol{k}. \tag{2.24}$$

A large number of k-points is required to accurately resolve this sum [32, 33]. In order to reduce the number of k-points, one replaces the step function with a smoothing function $f(\epsilon_{n\boldsymbol{k}})$ to smear out the integrand in k-space. Chosen right, the numerical integration of such a continuous function is much more effective while introducing only small errors.

A problem with the introduction of the smearing factor is that the total energy functional discussed in Section 2.4.2 is no longer minimal for the ground state. This is because the smearing in effect can be seen as introducing a temperature T to the system, whereas the original problem is to find the ground state at 0 K. Independent publications by Wentzcovitch et al. [34] and Weinert and Davenport

[35] presented a solution by showing that the free energy quantity

$$F[\rho] = E[\rho] + \sum_n k_\mathrm{B} T S(f_n) \tag{2.25}$$

is minimized by the ground state electron density ρ_0, even when E is not. This enables finding the ground state electron density through minimization of F and then the ground state energy energy E_0 by extrapolation of the free energy F to $k_\mathrm{B}T \to 0$.

2.5.6 Electronic and Ionic Relaxation

As mentioned earlier, VASP solves the Kohn-Sham equations for a system subject to periodic boundary conditions. As touched upon in Section 2.4.3, an algorithm may define the stopping criterion as when the total energy differs by less than some threshold value between iterations. This process is referred to as the electronic relaxation.

So far this chapter has focused on the problem of finding the minimum energy configuration of a set of electrons given a distribution of nuclei. However, many applications are concerned with the minimum energy distribution of both the electrons and the nuclei, that is *ionic relaxation*. The atoms are moved iteratively according to mutual forces and the self consistency loop is stopped when forces are below a certain limit F_max. It is therefore necessary for VASP to know the forces on the nuclei, i.e. the Hellmann-Feynman forces,

$$\boldsymbol{f} = -\boldsymbol{\nabla}_m E, \tag{2.26}$$

where E is the total system energy given a distribution of nuclei and electrons, $m \in 1 \ldots M$ and $\boldsymbol{\nabla}_m$ is the gradient operator with respect to positional components of nucleus m. However because of the introduction of partial occupancies, E is not readily available during simulation. Instead one has the smeared energy expression of Equation 2.23. This is where the free energy expression 2.25 comes in again. Wentzcovitch et al. [34] and Weinert and Davenport [35] showed that the Hellmann-Feynman forces of F are zero at the ground state. Thus, ionic relaxation can be performed by iteratively performing electronic relaxation before moving the nuclei according to the forces

$$\boldsymbol{f} = -\boldsymbol{\nabla}_m F, \tag{2.27}$$

where F is given by Equation 2.25. VASP can use numerical methods such as the conjugate gradient or the quasi-Newton methods to search the configuration space of R^M ionic positions for the ground state.

Chapter 3

Modeling and Methodology

3.1 Motivation

The goal of the present study is to calculate the atomic displacement field around β'' to obtain related properties, such as misfits and strains, and compare with previous experimental and theoretical studies. Near the precipitate-matrix interface of β'', atoms are displaced significantly, which means that a quantum mechanical description is necessary to predict their mutual forces. Comparing with a fully linear elastic treatment of the atomic interactions around a precipitate, a quantum mechanical treatment of the system picks up an additional contribution to the atomic displacement field, either positive or negative. This work attempts to capture this contribution by the use of the plane-wave DFT code VASP. An ionic relaxation procedure is employed as described in section 2.5.6.

Before presenting the current model in detail, a look is taken at the motivation for its use. Suppose one starts out with a full-size β'' precipitate enclosed in an infinite aluminium lattice. There are especially two problems in plane-wave DFT which make it difficult to realistically simulate this situation. The first is that the precipitate is not periodic, and must be contained within a periodic supercell as discussed in Section 2.5.1. The second problem is that the computational effort of DFT scales as N^q where $2 < q < 3$ and N is the number of electrons, which means that the practical limit for calculation with currently available computing resources is at a couple of hundreds to a few thousand atoms. In contrast, a full-scale β'' precipitate may contain more than ten thousand atoms, not even counting the surrounding host lattice. The question is then how to capture the behavior of

a precipitate with a very limited number of atoms.

The solution to these problems is to take advantage of the needle-like geometry of β'' and the small misfit along its habit directions. By assuming the precipitate to be entirely coherent along the $[0\,1\,0]_{\beta''}$ direction, it is sufficient to model a single unit cell thick cross-sectional slice of the precipitate. The super cell is made finite in the cross-sectional plane by cutting away the infinite aluminium lattice at some distance from the precipitate. Then, a surrounding vacuum is added as padding to mitigate the crosstalk between periodic repetitions of the system in the cross-sectional plane. Doing this, one goes from a full three-dimensional description of the problem to a semi two-dimensional one and the required number of atoms becomes manageable.

However, the vacuum-matrix interface presents a problem, because it is too close to the precipitate to contain the displacement field. Also, vacuum interface effects in the electronic structure may affect the simulation in unpredictable ways. Due to this, the present work fixes atomic positions in a boundary region at some radius from the precipitate. The displacement of these atoms are fixed to the solution predicted by linear elasticity. The rest of the atoms are allowed to relax during structural relaxation. The idea is to use a sufficiently wide annulus for the boundary region so that atoms inside and close to the precipitate experience being inside an infinite aluminium lattice.

3.2 Model Geometry

The model consists of four regions, contained in the simulation supercell. Figure 3.1 shows a schematic illustration of an $n_a \times n_c$ eyes precipitate model for reference. The outermost region is a vacuum which encloses what shall be referred to as the atomic slab. The regions are addressed here in order of decreasing proximity to the precipitate.

An $n_a \times n_c$ eyed precipitate is fit into a corresponding void in the aluminium lattice. The number of eyes used in each direction is sufficiently small that the entire precipitate fits into the aluminium lattice without misfit dislocations. The *precipitate radius* is the distance from its center of mass to its farthermost corner atom, as shown in Figure 3.1 and is given by

$$R_p = a\sqrt{13n_a^2/4 - 3n_a n_c + 5n_c^2}, \tag{3.1}$$

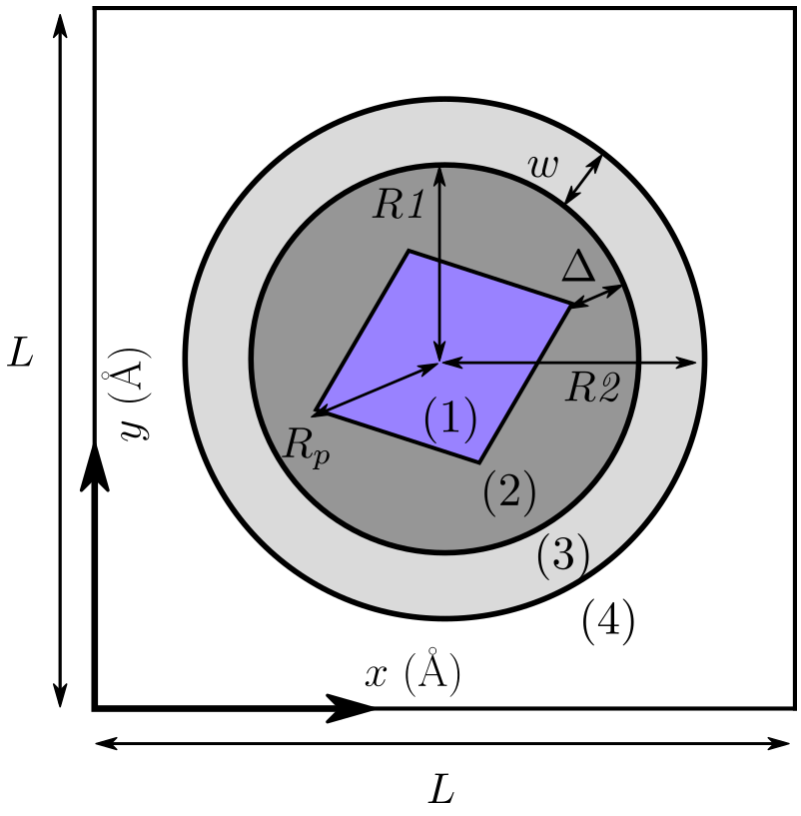

Figure 3.1: A two-dimensional schematic visualization of the model. The model is a one unit cell thick atomic cylinder. The square supercell has side lengths L. (1): Outline of the precipitate. (2): The inner region of relaxable Al atoms. (3): The static Al atoms displaced by LET. (4): Vacuum region to isolate periodic repetitions of the system. Important simulation parameters are indicated.

when all misfits are zero. Here, a is the zero Kelvin lattice constant of aluminium, determined through DFT, which will be discussed in Section 3.4.3.

The relaxable aluminium atoms enclose the precipitate and form a circularly shaped region about the precipitate. The distance from the outermost corner atom of the precipitate to the static region is

$$\Delta = R1 - R_p, \tag{3.2}$$

where $R1$ is the radius of the circle bounding the relaxable region. Δ must be determined such that the displacement field is allowed to develop sufficiently before reaching the static region. If Δ is set too small, atomic displacement in the relaxable region may be constrained too much by the static atoms in the annulus region. However, the total number of atoms and hence computational time grows with Δ,

so there is a limit on how large Δ can be. Thus, a convergence test is in order to determine the appropriate level of accuracy against computational cost.

The static region is shaped as an annulus defined by $R1 < r < R2$ where $R2$ is the outer radius of the atomic slab and r is the distance from the center of the slab. The width,

$$w = R2 - R1, \tag{3.3}$$

of the annulus determines how far the outermost relaxable atoms should be away from the vacuum-matrix interface. The vacuum and hence absence of atoms beyond the annulus means the particles in the relaxable region may not experience an infinite lattice environment. The atoms within the annulus are initially spaced like in a perfect aluminium lattice. They are then displaced by a compressive strain away from the precipitate from linear elastic calculations. The details of this coupling are presented below.

A vacuum region surrounds the circular slab in the x, y plane and is formed by cutting away all the aluminium atoms further than $R2$ from the precipitate center of mass. The shortest mutual distance between relaxable atoms is the radius of the relaxable region subtracted from the side length of the supercell and must be chosen so that periodic repetitions of the system do not interact significantly.

3.3 Coupling with Linear Elasticity

The LET displacement field for the precipitate comes from a simplified version of the modeling approach applied in the paper by Ehlers et al. [6]. The key difference is that they used DFT simulations for the precipitate interface, whereas the simulations used in this work employ LET exclusively.

The finite elements method (FEM) with orthotropic linear elasticity is used for the calculations. The model used is illustrated schematically in Figure 3.2. The precipitate in the DFT model is $n_a \times n_c$ eyes, bounded by $n_a/2 \times n_c$ unit cells of β'', with the shape of a parallelogram. Hence, the precipitate is modelled as a corresponding $w_\mathrm{p} \times h_\mathrm{p}$ parallelogram region with an angle of 105.3°, as seen in **b)**. The host matrix is 11 times larger than the precipitate, as illustrated in **a)**. The matrix and precipitate are represented by an approximately 200×200 grid of discrete nodes, where the grid lines were parallel to the precipitate directions $\boldsymbol{a}_{\beta''}$ and $\boldsymbol{c}_{\beta''}$. Elastic constants for the $Al_2Mg_5Si_4$ composition found by DFT in the

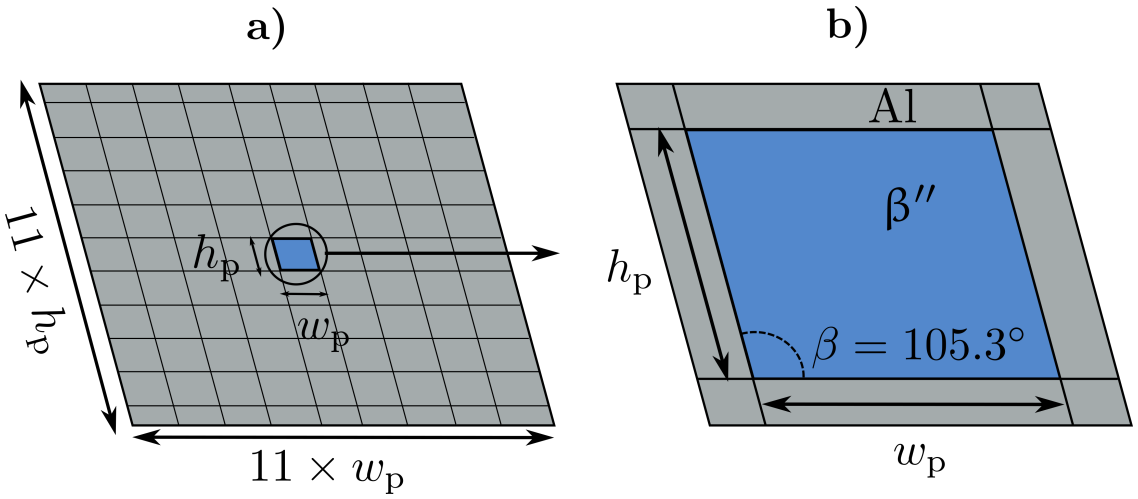

Figure 3.2: A figure illustrating the model used in linear elastic calculations for this work. **(a)**: The precipitate in orange has dimensions $w_\mathrm{p} \times h_\mathrm{p}$. The aluminium phase in grey is 11 times the dimensions of the precipitate along each grid direction. The nodes of the simulation are located at the intersections between line elements in the skewed grid. The number of nodes in the figure has been played down relative to the actual model. **(b)**: A zoomed in view of the precipitate in the model. Note that there are nodes inside the precipitate even though they have been omitted from the figure.

paper [26] are used. The calculations were performed strictly in two dimensions under the same assumption that $m_c = 0$.

The elastic field about the β″ precipitate is determined by following Eshelby's [36] approach. Conceptually one may view the process as follows: the precipitate is cut out of the host matrix and relaxed to the bulk state. An appropriate compressive displacement field is applied to the precipitate surface so that it fits the hole in host matrix. The surface nodes of the void are merged with their node counterparts on the precipitate. Subsequently, the entire system is relaxed through finite element calculations. The displacement field is discretely defined on the simulation nodes.

The linear elastic displacement field obtained had to be rotated about the z axis before applying it to the present atomic model. As Figure 3.2 shows the simulation by FEM was carried out with the precipitate $\boldsymbol{a}_{\beta''}$ vector along the x axis. The x, y components of each position and displacement were transformed by the following

transformation matrix

$$T = \frac{1}{a_{\beta''}} \begin{pmatrix} 2 & -3 & 0 \\ 3 & 2 & 0 \\ 0 & 0 & a_{\beta''} \end{pmatrix}. \tag{3.4}$$

The linear elastic displacement field obtained had to be interpolated before applying it to the atoms in the annulus of the present model. This is due to the displacement field being defined at nodes which do not directly correlate to atomic positions. A piecewise cubic polynomial interpolation of the displacement field was performed by a Clogh-Tocher scheme [37] using the griddata function [38] in the numerical package SciPy for Python. From this the displacement field at all positions in the atomic slab could be obtained, importantly for the atoms in the static region.

The interpolated displacement field was applied to all atoms in the slab by vector addition of the displacement field $\boldsymbol{u}_i$ at atom i and the atomic coordinate $\boldsymbol{r}_i$:

$$\boldsymbol{r}_i' = \boldsymbol{r}_i + \boldsymbol{u}_i, \tag{3.5}$$

where the index i runs over all the atoms and $\boldsymbol{r}_i'$ is the coordinate in the strained state. The displacement field was applied to all atoms rather than only those in the annulus because this was assumed to bring nearly all atoms closer to their equilibrium positions. This may reduce the number of necessary steps in the ionic relaxation, implying fewer electronic relaxation steps, effectively reducing the computational time needed.

3.4 Considerations

The present method of employing a coupling with LET to reduce the necessary number of atoms in the cross-sectional plane differs from previous atomistic modeling approaches to precipitates in that it focuses particularly on capturing a more accurate description of the atomic displacement field. Previous DFT studies of β″ have focused on the energetics [39] and morphology [21] of its formation, determination of the formula unit [5], configuration of the host-matrix interface [27] and energy barriers [40]. Most of those calculations are performed on bulk β″, single solute elements in an aluminium matrix or narrow interface supercells and do not take into account the precipitate cross-section surrounded by the host matrix. Such

studies obviously will not be able to capture the precise evolution of the strain field radiating from a precipitate.

So far only a few previous works have considered a complete precipitate cross-section in the host matrix. Ehlers et al. [26, 6] developed a multi-scale atomistic modeling scheme which combined LET calculations for bulk behavior with DFT calculations on the matrix-precipitate interface and expanded it from two dimensions to three in [41]. If the method in the present work is expanded to calculate energies, the results may be used to compare results obtained by Ehlers. Ninive et al. [8] modeled by DFT a precipitate cross-section in periodic aluminium supercells consisting of $12 \times 12 \times 1$ primitive aluminium cells to calculate formation enthalpies for different compositions of β'' and quantified the strain field surrounding the precipitates. The strain field obtained by Ninive [8] is effectively the strain field from an infinite number of densely spaced precipitates along the $\{0\,0\,1\}_{\mathrm{Al}}$ plane. It was reported to fall exponentially with the distance from the precipitate, which may be caused by the clearly unrealistic boundary conditions in this case because atomic displacement within the slab must be expected to be damped by the mutual interactions between the periodically repeating precipitates.

The use of atomic slab models with linear elastic boundary conditions has been more common in modeling of dislocation cores [42, 43, 10], but to the best of the current author's knowledge these methods have not been applied to precipitate modeling approaches thus far. One reason for this could be that modeling of entire precipitates of realistic size in DFT requires a greater number of atoms than a single dislocation and has therefore been more unachievable until the advent of increased computing power in recent years.

The hypothesis of this work is that the development of the displacement field close to the precipitate can be significantly improved compared to the previous atomistic models by letting the inner, relaxable region 'see' the displacement of atoms outside it. There are a few assumptions at play, discussed in the following sections.

3.4.1 Inner Region

First, one assumes that the true field surrounding the precipitate approaches rapidly the linear elastic solution in the relaxable region and that clamping their difference to zero in the fixed annulus introduces negligible errors within the relaxable area.

Setting Δ too small will constrain the inner field. Since the true solution to the interface field is unknown, it is impossible to know the evolution of the relative difference between it and the linear elastic field. The absolute value of the fields may even differ by a large relative factor far from the precipitate albeit both values should be small. In that case it would be best to couple the two systems and perform some sort of self-consistency cycle until the fields converge at the boundary. However, that is beyond the scope of this work and the important thing is that the LET field is an educated guess based on a higher level of approximation than DFT. This means it is a decent initial starting point and should at least yield more reliable estimates for the displacement and strain than previous models given that the errors introduced from other modeling assumptions are sufficiently small.

3.4.2 Fixed Atoms

It is assumed that fixing the annulus atoms to the linear elastic positions is sufficient to make the atoms in the inner region experience being in an infinite aluminium lattice. This assumption requires that the mutual interactions between pairs of atoms at a distance w in aluminium are negligible. It seems reasonable that such interactions should decay rapidly with the number of included nearest neighbors, as these are essentially quantum mechanical forces between neutral atoms. An additional effect arising at the matrix-vacuum interface is an abrupt reorganization of the electronic density which produces large forces at the outer boundary of the static region. These forces decay rapidly moving into the static region and are expected to be sufficiently small even for a narrow annulus. However, since the above assumptions do not say anything quantitatively about the width necessary to mitigate the above effects, a formal study of the width is needed.

In a preliminary investigation of the proposed model leading up to the present study, Ofstad [44] concludes that relaxation results should be fairly converged for $w > 10\,\text{Å}$. However, the present work will revisit that discussion with some new and more nuanced observations. The previous work studies the necessary width w of the annulus region by a convergence test of atomic displacement between subsequent atomic relaxation runs with increasing w. The work studies the displacement field surrounding a single β'' formula unit. Because the 1×1 precipitate is symmetrically equal in the $[1\,0\,0]_{\text{Al}}$ and $[0\,1\,0]_{\text{Al}}$ directions the surrounding field should be equal with respect to rotations of $\pi/2$. However in the preliminary work, a linear elastic

field made for larger precipitates, only symmetric with respect to rotations of π, is erroneously applied, and causes the relaxed state to be physically unreasonable. For this reason it is seen as necessary to revisit the discussion of w in the results and discussion chapter.

3.4.3 Important Parameters

For the consistency of the simulations, the present work uses the lattice constant $a = a_{\mathrm{DFT}}$ for aluminium determined by density functional theory, rather than the experimental lattice parameter a_0 of aluminium. This ensures that during simulation, the interatomic forces between atoms in a perfect aluminium lattice will be balanced at the lattice parameter a. The preliminary work by Ofstad [44] determined the DFT lattice parameter by fitting of unit cell energies to the Birch-Murnhagan equation of state. The value was found to be $a_{\mathrm{DFT}} = 4.046\,\text{Å}$, and is used throughout this work.

As mentioned in the theory chapter, the user of DFT should perform convergence tests on the total energy as a function of the cut-off energy in the plane-wave expansion and the density of k-points. For the current work values are taken from Ofstad [44] which determined appropriate values for these parameters. All parameters used are formally presented in Section 3.5.

3.5 Methodology

DFT Details

VASP was used for density functional theory calculations. The projector augmented-wave method (PAW) [45, 46] was used in combination with the generalized gradient approximation (GGA) by Perdew, Burke and Ernzerhof (PBE) for the core states and the exchange-correlation potential. The partial smearing of the Fermi-level was performed with a first order Methfessel-Paxton scheme [47].

Ionic relaxation was performed with the conjugate gradient algorithm, and the self-consistency loop was stopped according to a maximum force criterion as described in Section 2.5.6. The force criterion $F_{\mathrm{max}} < 0.1\,\mathrm{eV\,Å^{-1}}$ was used for one series of convergence tests. More accurate simulations used the quasi-Newton method with a stricter requirement of $F_{\mathrm{max}} < 0.01\,\mathrm{eV\,Å^{-1}}$. The simulations used a gamma-

point centered k-point mesh with $1 \times 1 \times 9$ k-points along the cardinal directions in the reciprocal space so that the maximum k-point spacing is $0.18\,\text{Å}^{-1}$. The energy cut-off was set to 400 Å.

LET Boundary Conditions

Simulations with linear elasticity were performed by the finite elements method on the commercial package LS DYNA [48] [†]. The linear elasticity simulations were performed assuming a homogeneous medium, and are therefore scale independent. Hence, the LET displacement field is the same up to a linear scaling factor for models with the same aspect ratio of precipitate eyes. For this reason, the same data sets were used for the displacement field in simulations with precipitates of equal aspect ratio. For each model created, displacement field data with the appropriate aspect ratio was scaled to fit the current precipitate. As a concrete example, the linear elastic data for an 8×8 precipitate was used in the 2×2, 3×3, 4×4 and 5×5 simulations by DFT.

3.5.1 Convergence Test of w

Four simulations were performed, the first with $w = 7\,\text{Å}$, the second to fourth with increasing w from 8 Å–12 Å by steps of 2 Å. The stopping criterion for ionic relaxation was set to $F_{\max} < 0.01\,\text{eV}\,\text{Å}^{-1}$.

3.5.2 Convergence Tests of Δ

Separate convergence tests were performed for precipitate sizes of 2×2 eyes and 3×3 eyes. The initial test was performed with a low force criterion of $F_{\max} < 0.1\,\text{eV}\,\text{Å}^{-1}$. Simulations were performed with increasing w by 1 Å steps from 2.57 Å to 11.57 Å. The next convergence test was performed with $F_{\max} < 0.01\,\text{eV}\,\text{Å}^{-1}$. w was incremented by 2 Å intervals from 6.57 Å to 10.57 Å for the 2×2 precipitate. For the 3×3 precipitate, w was incremented by the same amount from 6.57 Å to 12.57 Å.

[†]Simulation results supplied by Stephane Dumoulin, SINTEF.

3.5.3 Realistically Dimensioned Precipitate Models

Simulations were performed for a range of precipitate sizes reported experimentally in [9]. The sizes were 4×4, 4×5, 5×3, 5×4 and 5×5.

For each model an appropriate linear elastic displacement field was calculated and applied as explained earlier. Each precipitate model used $\Delta = 6.57\,\text{Å}$ and the width of the static region was set to $w = 7\,\text{Å}$, with the exception of 5×3, for which it was $w = 8\,\text{Å}$. The force requirement was set to $F_{\max} < 0.01\,\text{eV}\,\text{Å}^{-1}$.

Chapter 4

Results and Discussion

First, a note on terminology. The results are obtained on a per-simulation slab basis as relaxed atomic positions. When speaking about subsequent steps in convergence tests of either w or Δ, it should be taken to mean those simulations sorted by order of increasing w or Δ. Atoms which are associated with the same lattice point in the aluminium lattice relative to the precipitate are considered to be the same atom, just in a different simulation. When talking about the *displacement* between subsequent simulations, what is meant is the vector length between the relaxed positions of the same atom in separate simulations. When talking about the *displacement field*, what is meant is the atomic displacement in the relaxed state, relative to the perfect aluminium lattice.

4.1 Convergence Test of w

Figure 4.1 **a)** shows the atomic displacement in the inner region between subsequent relaxed configurations for increasing w. It is clear that the maximum atomic movement between subsequent relaxations is 0.033 Å, less than a percent of the aluminium lattice parameter. On average the atoms move by approximately 0.011 Å from one relaxation to the next, which is about 0.3% of the aluminium lattice constant, a. The average displacement changes insignificantly with respect to w. The maximum displacement between subsequent relaxations displays a weakly decreasing trend. However, inspection showed that the maximally displaced atoms corresponded to regions near the precipitate. Due to the distance from the static region, the interior part near the precipitate is expected to be least sensitive to

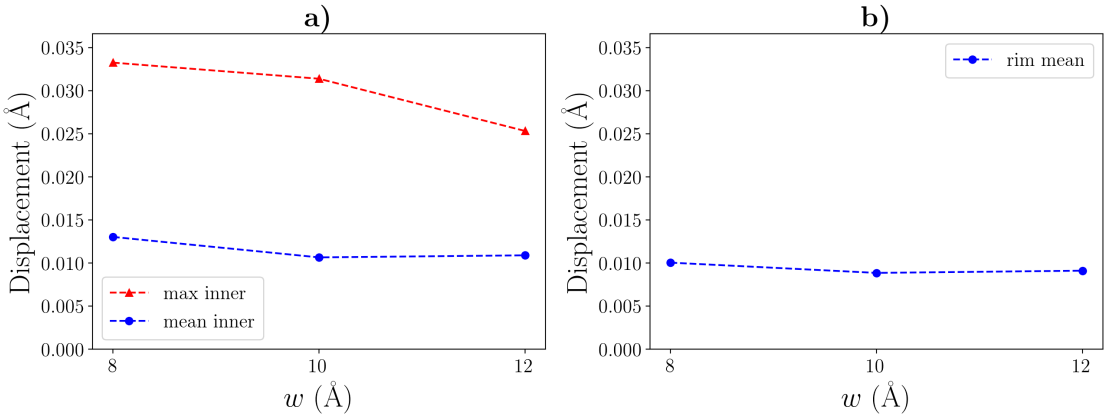

Figure 4.1: Mean and max values of the norm of the vector difference of atomic positions in subsequent relaxed configurations for the w convergence test with $F_{\max} < 0.01\,\mathrm{eV\,Å^{-1}}$. This means each successive data point in w uses information from the relaxed slab from the previous value of w. **a)**: In red triangles, the maximal displacement over the inner region. In blue circles, the mean displacement. **b)**: The mean displacement taken over the rim.

changes in w. These atoms are not likely to experience the effects of not being in an infinite aluminium lattice as strongly as those on the rim. Hence, the decreasing trend of the maximum displacement is likely not a sign of convergence.

The observed atomic displacement between simulations may be explained by the force criterion $F_{\max}$. To make the discussion simple, imagine a single atom being displaced from its least-energy position while all other atoms are kept static. Surrounding its energetic minimum position is a small region within which the forces on the particle will be less than $F_{\max}$. Then as soon as the particle falls within that region, the relaxation procedure is stopped. Thus the atom may end up anywhere within that region depending on the exact behavior of the minimization algorithm used. Further, if the starting point is changed slightly, the atom will likely relax to another position within the region. For the full system of relaxable atoms, the situation is even more complicated due to the fact that all atoms are allowed to relax, but the basic behavior is the same. Atoms will come to rest somewhere in the vicinity of their least-energy positions, and the starting point will affect the final relaxed result. In this way, the distribution of atoms in the vicinity of their equilibrium position is similar to a random variable in that it is impossible for the user to predict where the atoms will relax to. In the convergence test on w, the

starting point is different due to the different number of atoms in each subsequent simulation. The perfectly relaxed positions were estimated by taking the average of the relaxed atomic positions. Then the positional standard deviation in the position of each atom in the x direction is given by

$$\sigma = \sqrt{\frac{\sum_{i=1}^{N}(x_i - \bar{x})}{N-1}}, \tag{4.1}$$

where $\bar{x}$ is the average and N is the number of simulations in the w convergence test. The standard deviation was calculated, and the mean of this quantity taken over all the atoms was approximately 0.01 Å in both the x and y directions. Thus, it appears that atomic positions are determined within approximately 0.01 Å in the x and y directions for $F_{\max} < 0.01\,\mathrm{eV\,\AA^{-1}}$ and that fluctuation with respect to w is below that limit.

As mentioned previously, the atoms which are expected to be the most affected by the choice of the annulus width are the ones on the outer rim of the inner region, due to their proximity to the annulus. The displacement of these atoms between subsequent relaxations has been plotted in Figure 4.1 **b)**. The mean atomic displacement is approximately 0.008 Å, which is almost the same as for the average over the entire inner region. There is no decreasing trend in this plot either. Thus, in conclusion the fluctuation of the atomic positions between simulations is likely caused by other factors such as the force criterion used, rather than the variations in the annulus width. Hence it was deemed sufficient to use $w = 7$ Å for further simulations.

The misfit parameters m_a and m_c were calculated to assess how much they could vary due to the observed variation of atomic positions. The average misfits were $m_a = 4.12\%$ and $m_c = 5.36\%$. The misfits varied by 3.5% (m_a) and 6% (m_c) relative to the misfits themselves, so the variation was small. This shows that variations of a few percent can be attributed to the positional inaccuracy at $F_{\max} < 0.01\,\mathrm{eV\,\AA^{-1}}$.

4.2 Convergence Tests of Δ

Figure 4.2 shows the mean difference between the LET field and the relaxed positions on the rim of the relaxable region for the convergence test with $F_{\max} < 0.1\,\mathrm{eV\,\AA^{-1}}$. The graphs show a marked decrease with the first few values of Δ but do not decrease significantly for $\Delta > 6.57$ Å. Since the displacement field from

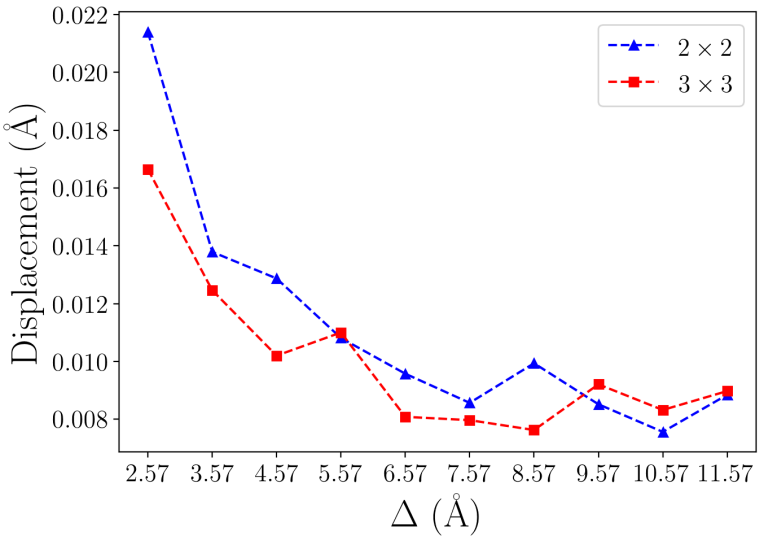

Figure 4.2: The mean norm of the vector difference between the atomic positions before and after relaxation taken over the rim region of each consecutive atomic slab in the first Δ convergence test. In blue triangles, evaluated for the 2×2 precipitate models. In red squares, evaluated for the 3×3 models.

both DFT and LET should approach zero far away from the precipitate, so should their difference. However, as noted, the graphs do not decrease significantly after $\Delta > 6.57\,\text{Å}$. To investigate convergence further, additional simulations were performed with $F_{\text{max}} < 0.01\,\text{eV Å}^{-1}$ to look for convergence beyond $\Delta = 6.57\,\text{Å}$. Figure 4.3 is the same as Figure 4.2 for the strict force requirement. The mean difference in atomic position before and after relaxation decreases somewhat for the 2×2 precipitate in this convergence test. However for the 3×3 precipitate the trend is opposite, the displacement field increases for the first three data points and drops by 0.02 Å for the last. The results indicate that increasing the force requirement does not significantly change the difference between DFT and LET on the edge. One can only assume the atoms to come to rest within some radius of the LET positions. This is caused by the atoms never really relaxing beyond a positional accuracy of approximately 0.01 Å as observed for the w convergence test.

Due to the difference between DFT and LET decreasing to approximately 0.01 Å for $\Delta = 6.57\,\text{Å}$ it was decided that this value would be sufficient for all further simulations in this work. To obtain a rough estimate of the error in this assumption, the average displacement by increasing radial distance to the precipitate has been

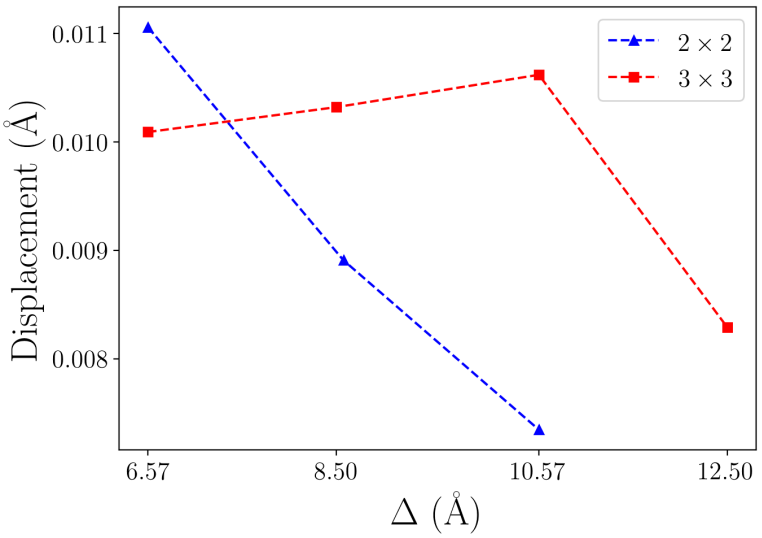

Figure 4.3: The mean norm of the vector difference between the atomic positions before and after relaxation taken over the rim region of each consecutive atomic slab in the second Δ convergence test. In blue triangles, evaluated for the 2×2 precipitate models. In red squares, evaluated for the 3×3 models.

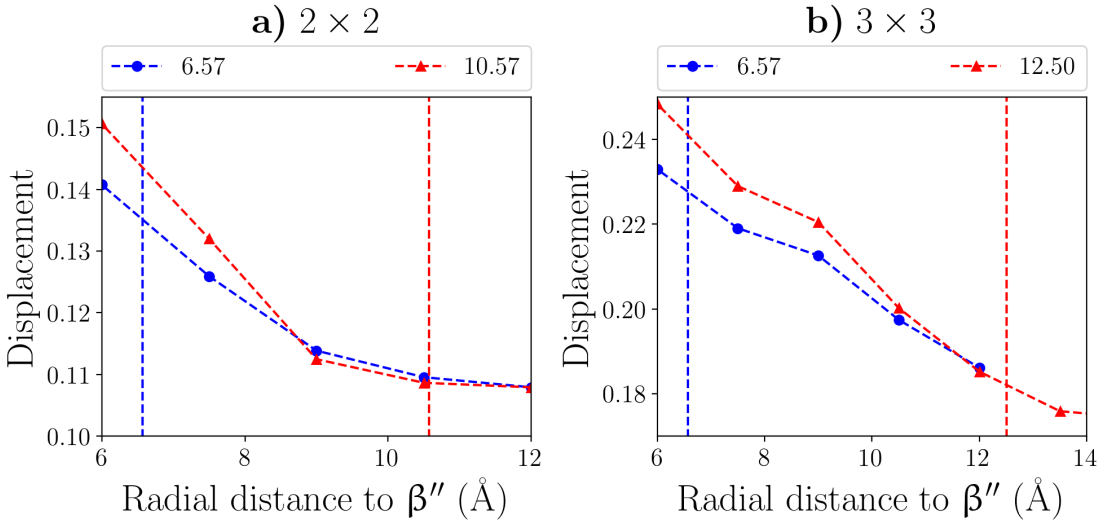

Figure 4.4: The magnitude of the DFT displacement field averaged over all atoms at a radius Δ from the center of the precipitate plotted for increasing Δ. In red triangles, the displacement field for the largest slabs. In blue circles, the displacement field for the smallest slabs. **a)**: Plot for the 2×2 precipitate. **b)**: For the 3×3 precipitate.

plotted in Figure 4.4 **a)** (2×2) and **b)** (3×3) using the data obtained with a strict force requirement. Notice that the curves represent the linear elastic displacement field to the right of their respective Δ. Hence the blue and red curves, indicated by circles and triangles respectively, will be equal to the right of the red vertical lines. In the case of the 3×3 precipitate the blue curve does not go that far because $\Delta = 12.5\,\text{Å}$ lies in its vacuum region. One can see that the development of the displacement field is qualitatively similar for different Δ, differences being in the order of $0.01\,\text{Å}$. This was found to be true for the rest of the graph as well. The difference in displacement field strength between the largest and smallest slabs at $\Delta = 6.57\,\text{Å}$ was found to be $0.007\,\text{Å}$ and $0.013\,\text{Å}$ for the 2×2 and 3×3 precipitates, respectively. Thus, clamping the displacement field to the linear elastic value at $\Delta = 6.57$ seems to systematically underestimate the displacement field strength relative to the largest slab by roughly these values, and notably more for the 3×3 precipitate.

The misfits m_a and m_c were calculated for the different inner region sizes to investigate if there was an observable relation between misfits and differences in displacement field strength. Misfits in the $\boldsymbol{a}_{\beta''}$ and $\boldsymbol{c}_{\beta''}$ directions vary by 2% and 1.4% (3×3) and 0.25% (m_a) and 3.17% (2×2), respectively. No significant trend could be observed. Further, the observed variations are within the variations of 3% and 6% for the w convergence test, meaning that they could be entirely caused by the inherent fluctuation of atomic positions. For this reason, the misfits are likely not significantly affected by the change in the magnitude of the displacement field associated with the clamping at $6.57\,\text{Å}$, further justifying the choice of parameter.

4.3 Importance of $F_{\max}$

It is important to use a requirement on the forces of at least $F_{\max} < 0.01\,\text{eV}\,\text{Å}^{-1}$ for all simulations of large atomic slabs such as those in the present work.

Figure 4.5 is the same as 4.1 **b)** except with a less strict force criterion of $F_{\max} < 0.1\,\text{eV}\,\text{Å}^{-1}$. It can be seen that the atomic displacement is lower in both the graphs relative to 4.1. This actually indicates that atomic positions change *more* between subsequent simulations for a strict force requirement than for a weak force requirement. This seemed contradictory at first, because it was expected a stricter force requirement would reduce the amount of atomic displacement. To see exactly

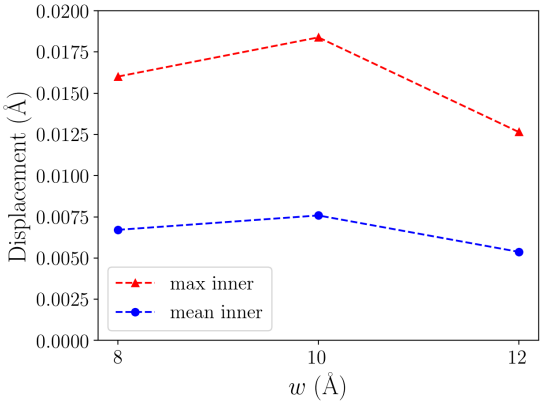

Figure 4.5: Mean and max values of the norm of the vector difference of atomic positions in subsequent relaxed configurations for increasing w in the w convergence test with $F_{\max} < 0.1\,\mathrm{eV\,\AA^{-1}}$.

what the difference is between using a mild and a strict force requirement, it is useful to look at the displacement of individual atoms. Figure 4.6 **a)** illustrates the difference in the atomic displacement field between the case of the strict force criterion and the weak criterion for $w = 8\,\text{Å}$. A significant portion of atoms move as much as 0.04-0.06 Å, 1% of a, due to the increase in $F_{\max}$. Figures 4.6 **b)** and **c)** are the components of **a)** in the radial and angular directions with respect to the slab center of mass. It is clear that most of the displacement occurs in the radial direction and least in the angular direction. The radial component is mostly positive, so the relative displacement is mainly outwards from the precipitate, indicating that when $F_{\max}$ is too large, the aluminium lattice does not properly accommodate the displacement field generated by the precipitate. This may be caused by the way the structural relaxation is performed. For a soft force requirement, the atoms are closer to an acceptable configuration from the start, and do not require a lot of movement before the algorithm finds a configuration that obeys the force criterion. This way, the atoms are not displaced so far from their initial positions in the relaxed state. Hence, different relaxed states are correspondingly more similar. Making the force criterion stricter, the algorithm must move atoms more in the search for the optimal configuration. While the relaxed structures are closer to the true ground state, incidentally they also happen to be less similar than predicted by the soft force requirement.

It can be observed from Figure 4.6 that the displacement is larger close to the

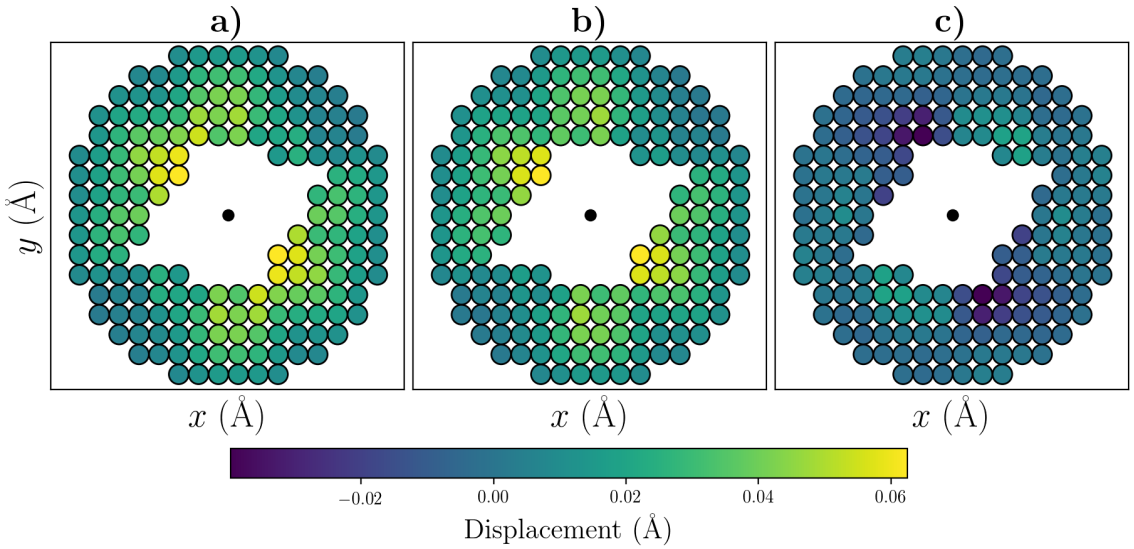

Figure 4.6: The vector difference between atomic positions before and after relaxing forces from $F_{\max} < 0.1\,\mathrm{eV\,\AA^{-1}}$ to $F_{\max} < 0.01\,\mathrm{eV\,\AA^{-1}}$. **a)**: The magnitude. **b)**: The radial component with respect to the precipitate center, which is indicated by a black dot. The displacements are mostly positive, that is, pointing away from the precipitate. **c)**: The angular component relative to the precipitate center.

precipitate. This suggests the precipitate also expands by a significant amount when going from a slack to a strict force requirement. Indeed, the relative increase in m_a and m_c was 4% and 10% for the strict force criterion, which is more than the variations observed between subsequent simulations in the w convergence test. This further attests to the fact that there is a systematic difference between simulations with a high force criterion and a low force criterion. The behavior of increased radial displacement, as in figure 4.6, was observed for all the relaxations performed in the current work when comparing relaxed positions for different force criterions. This fact makes it clear that the convergence of atomic positions with respect to the force requirement $F_{\max}$ should be tested. This was not done due to time constraints close to the approaching deadline for submission of the present work. That being said the force criterion $F_{\max} < 0.01\,\mathrm{eV\,\AA^{-1}}$ is the same as used in Ninive et al. [8], which is used for comparison. Finally, it is noted that because there was a significant radial displacement of atomic positions between $F_{\max} < 0.1\,\mathrm{eV\,\AA^{-1}}$ to $F_{\max} < 0.01\,\mathrm{eV\,\AA^{-1}}$, it is expected that making the force requirement even stricter should lead to a mostly radial displacement which is stronger near the precipitate.

If this assumption is correct, the calculated misfits in the current work should be somewhat underestimated.

4.4 Misfits

Table 4.1: Misfit values m_a and m_c for β″ precipitates of different cross-sectional sizes. On the left are the values calculated in the present work. Misfits from other works have been included for reference. For each reference value, the difference with the presently calculated misfit is included in parentheses, except for the bulk misfits.

	DFT (Present)		ADF-STEM [9]		DFT [41] *		DFT [5] †	
Size	m_a (%)	m_c (%)	m_a (%)	m_c (%)	m_a (%)	m_c (%)	m_a (%)	m_c (%)
Bulk					4.91	5.85	6.15	5.25
5×5	3.94	4.76	3.36 (-0.58)	3.69 (-1.07)				
5×4	3.59	5.11	3.09 (-0.50)	4.61 (-0.50)	DFT/LET [49] ‡			
5×3	3.09	5.71	2.62 (-0.47)	4.54 (-1.17)	m_a (%)		m_c (%)	
4×5	4.25	4.32	3.59 (-0.66)	3.36 (-0.96)				
4×4	3.98	4.71	3.66 (-0.32)	4.29 (-0.42)	2.45 (-1.53)		3.07 (-1.64)	
3×3	4.04	4.89						
2×2	4.11	5.41						

Misfits were calculated by measuring the distance between the aluminium atoms on the midpoints of the precipitate-matrix interface in each of the directions $\boldsymbol{a}_{\beta''}$ and $\boldsymbol{c}_{\beta''}$. The calculated misfits can be found in Table 4.1. Computational and experimental results from other works have been included for reference.

The present misfits are smaller than previously reported values in bulk for $Al_2Mg_5Si_4$, except for two of the geometries. This is expected, because β″ is known to produce a displacement field which is positive radially outwards from the precipitate. Consequently, the matrix acts with a compressing force on the β″ precipitate.

*Obtained from TABLE III in that work.
†Obtained from Table 1 in that work.
‡Obtained from Table 1 in that work.

Bulk relaxations do not take into account this pressure, and so the relaxed lattice parameters will be less compressed in bulk than in the host matrix. There are two exceptions to this trend. m_c is larger than the bulk values for the 2×2 and 5×3 precipitates, $m_c = 5.41\%$ and 5.71% respectively. The former is somewhat extraordinary due to its small size. The present author has not been able to find direct reference to such small precipitates in experimental studies, but Ninive [8] reported the 2×2 precipitate unit cell to be larger than the one for 3×3, consistent with the present work (see discussion on misfit areas below for further details).

The large m_c for the 5×3 precipitate is explained by the Poisson effect. The precipitate responds to a larger cross-sectional aspect ratio in one direction by reducing the misfit along that lattice direction and increasing the misfit along the other direction. The Poisson effect arises because larger precipitate dimensions along one lattice direction increases the compression exerted by the surrounding aluminium lattice in that direction. This would lead to the analogue of a pressure increase inside the precipitate, but the precipitate expands in the other direction to cancel out the pressure differential analogue. For a high aspect ratio precipitate such as the 5×3 one, m_c should be larger the due to the large $\boldsymbol{a}_{\beta''}$ dimension, and this is precisely what is observed. The Poisson effect can be visualized by plotting the misfit ratio $R_{\mathrm{M}} = m_a/m_c$ as a function of the length ratio of the precipitate, R_{L}, given by Equation 2.2, as in Figure 4.7. The same has been done previously in [9], and for reference, the corresponding graph from that paper has been reproduced by using the misfit values reported therein as well as data from [49]. [9] also commented that the data (in red) showed a close to inverse proportionality between R_{L} and R_{M}. Indeed, for the data in that work, a least squares fit to a reciprocal function $R_{\mathrm{M}}(R_{\mathrm{L}}) = C/R_{\mathrm{L}}$ gives a value of the coefficient $C \approx 1.00$. The same procedure repeated with data in the current work gives $C \approx 0.93$, as can be seen in Figure 4.7. The fitting to the reciprocal function works quite well for both of these works, as the data points fall relatively close to the curve in both cases. In contrast, the data from [49] yields $C \approx 0.78$, and the fitted curve does not seem to describe the development of the data points very well. Returning to the data obtained in the present work, since $R_{\mathrm{M}}(1/R_{\mathrm{L}}) = C^2/R_{\mathrm{M}}(R_{\mathrm{L}})$, the misfit ratio m_a/m_c of a 4×5 precipitate should be $C^2 \approx 86\%$ of m_c/m_a for a 5×4 precipitate. In contrast, this relation was perfectly symmetrical between the $\boldsymbol{a}_{\beta''}$ and $\boldsymbol{c}_{\beta''}$ directions in the experimental study [9].

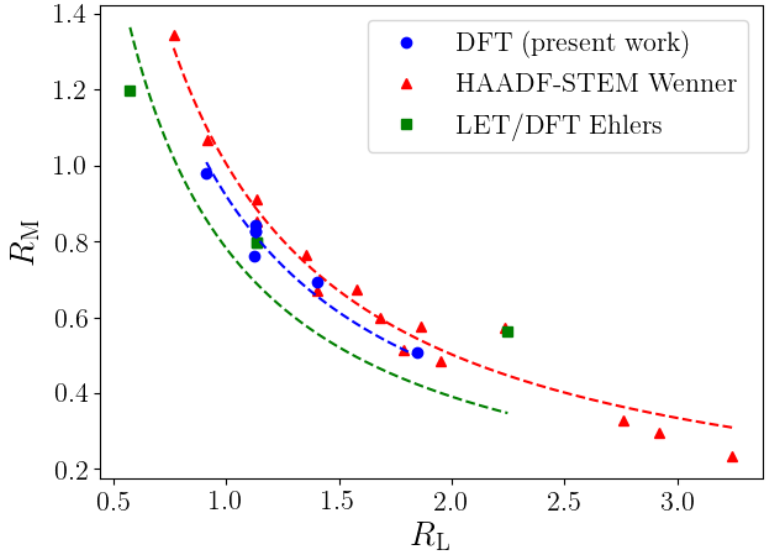

Figure 4.7: A plot of the misfit ratio $R_{\mathrm{M}} = m_a/m_c$ by the length ratio R_L (see Equation 2.2) of various precipitate dimensions. In blue circles, the data from the present work. In red triangles, data from Wenner and Holmestad [9]. In green squares, data from Ehlers et al. [49]. Each data set has been fitted by least squares to a reciprocal expression $R_{\mathrm{M}} = C/R_{\mathrm{L}}$ by varying the coefficient C. Values for the coefficient can be found in the text.

The misfits in the present work are comparatively larger by between 10%–30% relative to their experimental counterparts from [9]. Andersen et al. [20] measured $m_a = 3.82\%$ and $m_c = 5.25\%$ for a relatively large precipitate, and this observation is slightly closer to the values obtained in the current work. Another way to quantify the size of the precipitates is the relative misfit area. It is the fraction by which the β″ unit cell is expanded relative to when all misfits are zero. It is given by $A_{\mathrm{m}} = (1 + m_a)(1 + m_c) - 1$, assuming the precipitate retains the quadrilateral shape with straight precipitate-matrix interfaces. The large precipitate in [20] yielded $A_{\mathrm{m}} = 9.27\%$, and the present work obtains values between 8.76% and 9.75% for the various precipitate dimensions, averaging at $A_{\mathrm{m}} = 9.03\%$. This is in good agreement with the result from [20]. A_{m} decreases with precipitate size, with A_{m} being approximately 0.01 larger for the 2×2 precipitate than the 5×5 one. In contrast, Wenner and Holmestad [9] found A_{m} in average to be 7.18% with no clear dependence on precipitate dimensions. Hence, the present investigation suggests the precipitate unit cell shrinks slightly with increasing precipitate dimen-

sions, whereas the experimental study by Wenner and Holmestad showed no such correlation. The difference between the β″ unit cell dimensions in the present study and the experimental study decreases with precipitate size.

Comparing the misfit area with some other studies, the value for the 4×4 precipitate was reported to be $A_{\mathrm{m}} = 7.53\%$ in the pure DFT study by Ninive [8]. The combined DFT/LET approach by Ehlers [49] reported 5.6%. The present investigation obtained a value of 8.86%, whereas the experimental study of Wenner [9] reported 8.11%. Ninive's model does comes closest to the experimental study for this precipitate size. Further, Ninive reports values of $A_{\mathrm{m}} = 7.12\%$ (2×2) and $A_{\mathrm{m}} = 5.75\%$ (3×3). Notably, also these values are closer to the experimental results of [9] than those obtained in the present work.

If one assumes the misfits measured in [9] to be the ground truth, the current work is systematically overestimating the expansion of the precipitate. This could be caused by the Al matrix exerting less constricting force on the β″ particle than would be the case in a real alloy. Temperature effects may play a role in this, but this is entirely speculative. One could also hypothesize that the LET simulations overestimate the displacement field in the annulus region, and less so for larger precipitates. This would lead to a larger displacement field in the static region, effectively reducing the degree of constriction of the inner region and the precipitate during structural relaxation. However, this seems contradictory, as it is observed in the next section on strain that LET underestimated the strain field near the precipitate-host matrix interface significantly. Furthermore, the discussion on the force criterion, F_{max} concluded that the misfits are likely somewhat underestimated, in contrast to the overestimation which is actually observed. Ultimately, the observed discrepancy between experiment and theory could not be explained in the present investigation.

4.5 Strain

Figure 4.8 illustrates the discrete strain components ϵ_{xx} and ϵ_{yy} at each atomic position in the lattice for the 3×3 precipitate. The plots are qualitatively representative of the other precipitate sizes as well. Paying attention to the silicon atoms (silver grey) in **a)**, one sees that the most negatively strained Al rows correspond to the Si atoms on the [2 3 0] precipitate interfaces. Vice versa, the Si atoms on the

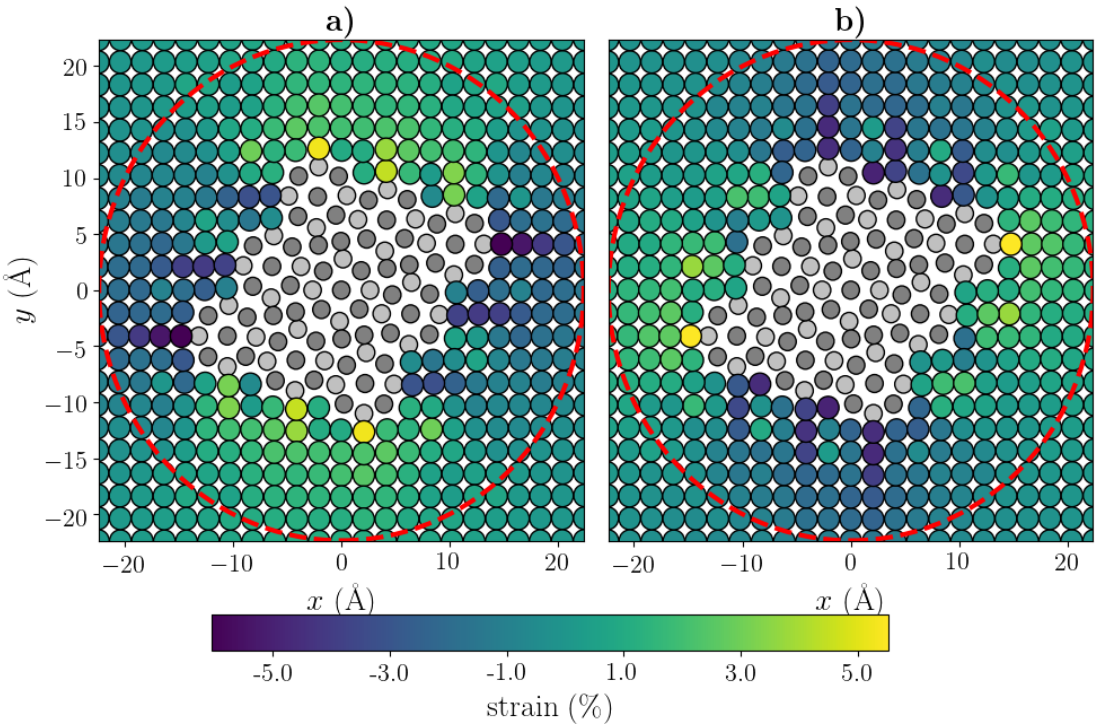

Figure 4.8: The discrete strain field, as explained in Section 2.4 for a 3×3 precipitate. The spheres indicate each atom, and the color indicates the strain value at each atom. The aluminium atoms of the precipitate which lie on the precipitate-host matrix interface, have been assigned a strain value and are colored according to the color bar as well. In dark grey, Mg atoms and Al atoms which do not belong to the aluminium lattice. In silver, Si atoms. The red, stippled line indicates the radius of the relaxable region, *R1*. **a)**: A plot of ϵ_{xx}. **b)**: A plot of ϵ_{yy}.

$[\bar{3}\,1\,0]$ of β'' coincide with the most positively strained atomic columns in the Al matrix. In particular, the largest magnitude of ϵ_{xx} occurs near the corners, right/left of symmetrically opposite Si atoms, whose x coordinates are the largest/smallest of any Si atom in the precipitate. ϵ_{xx} is mainly negative at the $[2\,3\,0]_{\mathrm{Al}}$ interfaces and positive at the $[\bar{3}\,1\,0]_{\mathrm{Al}}$ interfaces. ϵ_{xx} is notably more negative outward in the $[1\,0\,0]_{\mathrm{Al}}$ direction out from the interface Si atoms on the $[2\,3\,0]_{\mathrm{Al}}$ interfaces than in the surrounding lattice. This effect is not as strong on the other two interfaces, where the expansion of the lattice is more diffuse except for exactly at the interface. The same can be observed for ϵ_{yy}, atomic columns out from the Si atoms at the $[\bar{3}\,1\,0]_{\mathrm{Al}}$ interfaces being more compressed than the surrounding lattice.

Further insight can be obtained by looking at Figure 4.9 **a)**, which is an interpo-

lated plot of the strain field ϵ_{xx} from Figure 4.8 **a)**. It can be seen that the strain is negative inside two regions beginning at the two respective $[2\,3\,0]_{\mathrm{Al}}$ interfaces, and bounded by the 0% contour curves which almost connect to the four corners of the figure with the corners of the precipitate. These regions will simply be referred to as the right and left sides of the precipitate, corresponding to positive and negative x respectively. Correspondingly, $\epsilon_{xx} > 0$ above and below the precipitate. The interpolation of ϵ_{yy} has not been plotted, but in its case the behavior is similar, only this time with an opposite sign of ϵ_{xx} in the different regions surrounding the precipitate.

The above observations on the strain in the $[1\,0\,0]$ and $[0\,1\,0]$ directions in the aluminium lattice can be explained by the precipitate being expanded relative to the perfect aluminium lattice in the x and y directions respectively. The expansion of the precipitate in the x direction leads to compression of atomic rows to its right and left. Due to shear forces, atomic rows above and below the compressed atomic rows are also compressed slightly. This will lead to negative ϵ_{xx} on the left and right side of atomic rows that are situated off the precipitate in the y direction as well. This means these rows must expand in the middle to distribute compression and expansion evenly. Furthermore, the precipitate expansion in the x direction above and below the precipitate pulls atomic columns apart, leading to a positive strain component. The effect is naturally stronger near the precipitate interface, as atoms will seek to reduce deformation further away. The strain differences cancel out along the 0% isolines, which incidentally fall relatively close to the $\langle 1\,1\,0\rangle$ directions outwards from the precipitate. A similar explanation applies to the strain component ϵ_{yy}, in which case the expansion in the y direction leads to a negative value above and below the precipitate and positive to the right and left.

Figure 4.9 **b)** shows ϵ_{xx} given by pure LET. Together with **a)** one may compare the differences between pure LET and the combined DFT/LET approach. The contour curves are smoother for the LET data. This is expected, because the LET simulations assumed a continuous medium. It can be seen that the LET results underestimate the magnitude of the strain field at the precipitate interfaces. In particular, the aluminium atoms next to interface silicon atoms experience significant strain values of $|\epsilon_{xx}| \approx 6\%$. The corresponding values by LET are $|\epsilon_{xx}| \approx 3.5\%$, showing that LET significantly underestimates these strains. Even so, the strain is relatively similar for the two levels of approximation away from the interface.

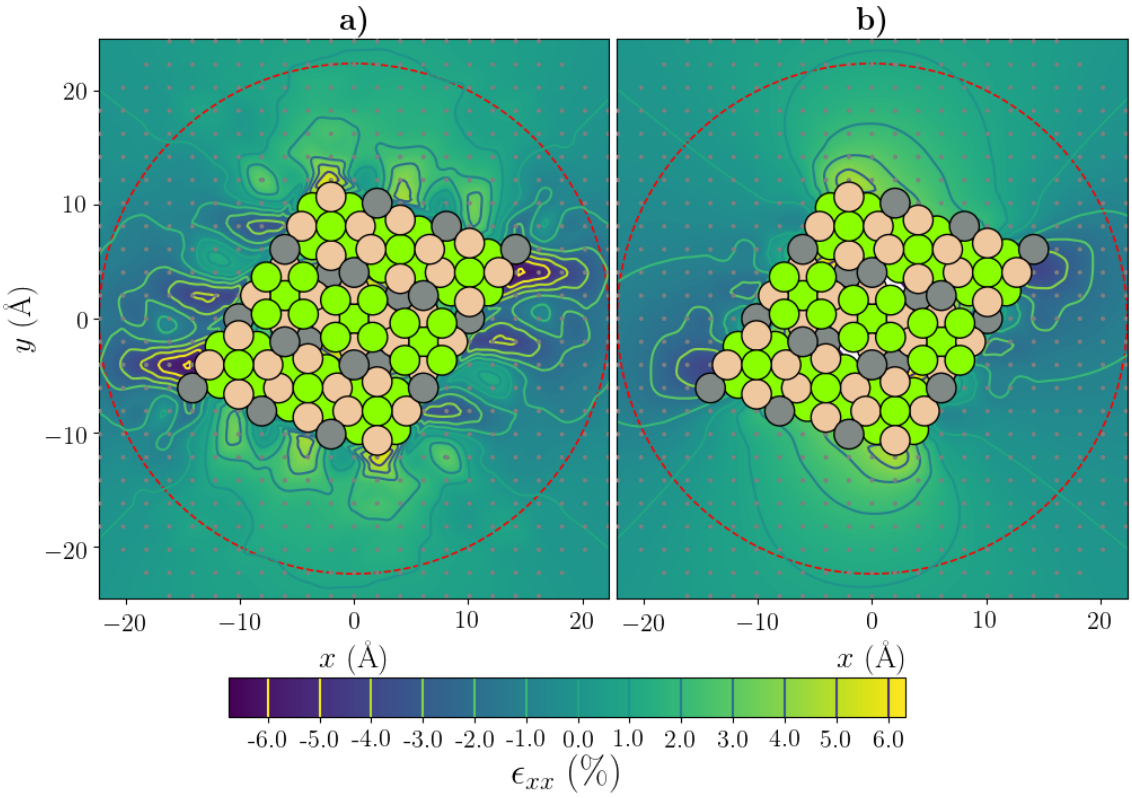

Figure 4.9: A cubic interpolation of the discrete strain component ϵ_{xx} for a 3×3 precipitate from Figure 4.8. **a)** shows the strain component given by combined LET boundary conditions and relaxation with DFT. **b)** is the strain from pure LET. The colors indicate the local strain. Contour curves are included with colors contrasting the background. The precipitate has been indicated. The other atoms have been indicated by small, grey dots. The stippled red line shows the extent of the region relaxed by DFT.

In comparison, Ninive et al. comment in [7] that the aluminium matrix was strained by up to 5% close to the precipitate-matrix interface, smaller by approximately 1% than the number observed in the present work. [7] also reports a near exponential decline in strain away from the precipitate-matrix interface. The strain field components ϵ_{xx} and ϵ_{yy} were reported to be $< 1\%$ at at 10 Å from the precipitate-matrix interface. Figure 4.10 was made for comparison with those results, and illustrates the strain field ϵ_{xx} at each atomic position away from the precipitate-matrix interface in the x direction taken at the atomic row of maximum strain magnitude. **b)** illustrates the line along which ϵ_{xx} was taken. As can be seen from the figure, the magnitude of ϵ_{xx} decreases almost linearly for the first four data points. Then at the annulus interface, the strain magnitude decreases more

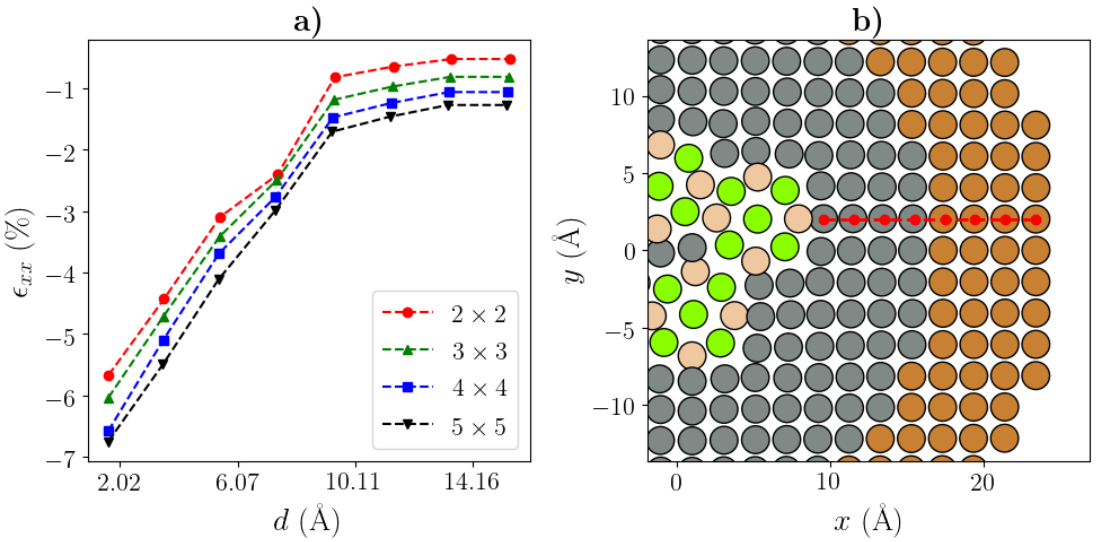

Figure 4.10: **a)**: A plot of ϵ_{xx} by the distance d from the precipitate along the row of maximal strain magnitude for four precipitate models. In red circles, 2×2, in green triangles 3×3, in blue squares, 4×4 and in black reversed triangles, 5×5. The four leftmost data points are taken between atoms relaxed by DFT, and the four rightmost data points are taken between static atoms in the annulus. **b)**: A plot illustrating which atoms have been measured in the 2×2 precipitate model. In grey, relaxable aluminium atoms, in brown, static atoms.

than between the previous data points before flatting out. If one were to draw a continuous function between the data points, its derivative would change significantly at the annulus interface. Further, in the 2×2 case the derivative seems to decrease slightly in the first four data points, before decreasing to the next and then increasing again. This erratic behavior seems to be caused by the LET boundary conditions. Due to the large changes in the derivative, it is clear that the development of ϵ_{xx} cannot be described very well by an exponential function. However, excluding the annulus data points, a fit can be made reasonably well. The fit for the 2×2 precipitate was $\epsilon_{xx} = c_0 \exp(c_1 x)$, with $c_0 = 24.2$ and $c_1 = -0.15$. These values fall quite close to the numbers from [7], $c_0 = 25.2$ and $c_1 = -0.2$. Evidently, the present combined DFT/LET approach and the pure DFT approach in [7] are comparatively similar in predictions of strain in relaxable region. The coefficients obtained for the present strain curves were slightly lower than in [7], meaning that the exponential fit decreases slower with respect to the distance from the precipitate. Last on the topic of comparison, the reader is referred to Figure 4.4, p.57

in Ninive et al. [11] for a visual comparison between the strain plots of the 2×2, 3×3 and 4×4 precipitate contour plots of ϵ_{xx}. The corresponding plots in the present work are found in Figure 4.9 **a)** and Figure 4.11 **a)** and **b)**. The plots are comparatively quite similar, and the strain values are almost indistinguishable by visual inspection. However, near the precipitate-matrix interface, there are some differences in strain magnitudes they tend to be stronger in the present work. This is consistent with the earlier discussion of misfits. It would seem natural that the larger precipitates of he present work lead to a larger strain close to the precipitate. Finally, Figures 4.11 **c)** and **d)** show the contour plots of the 4×5 and 5×3 precipitates respectively.

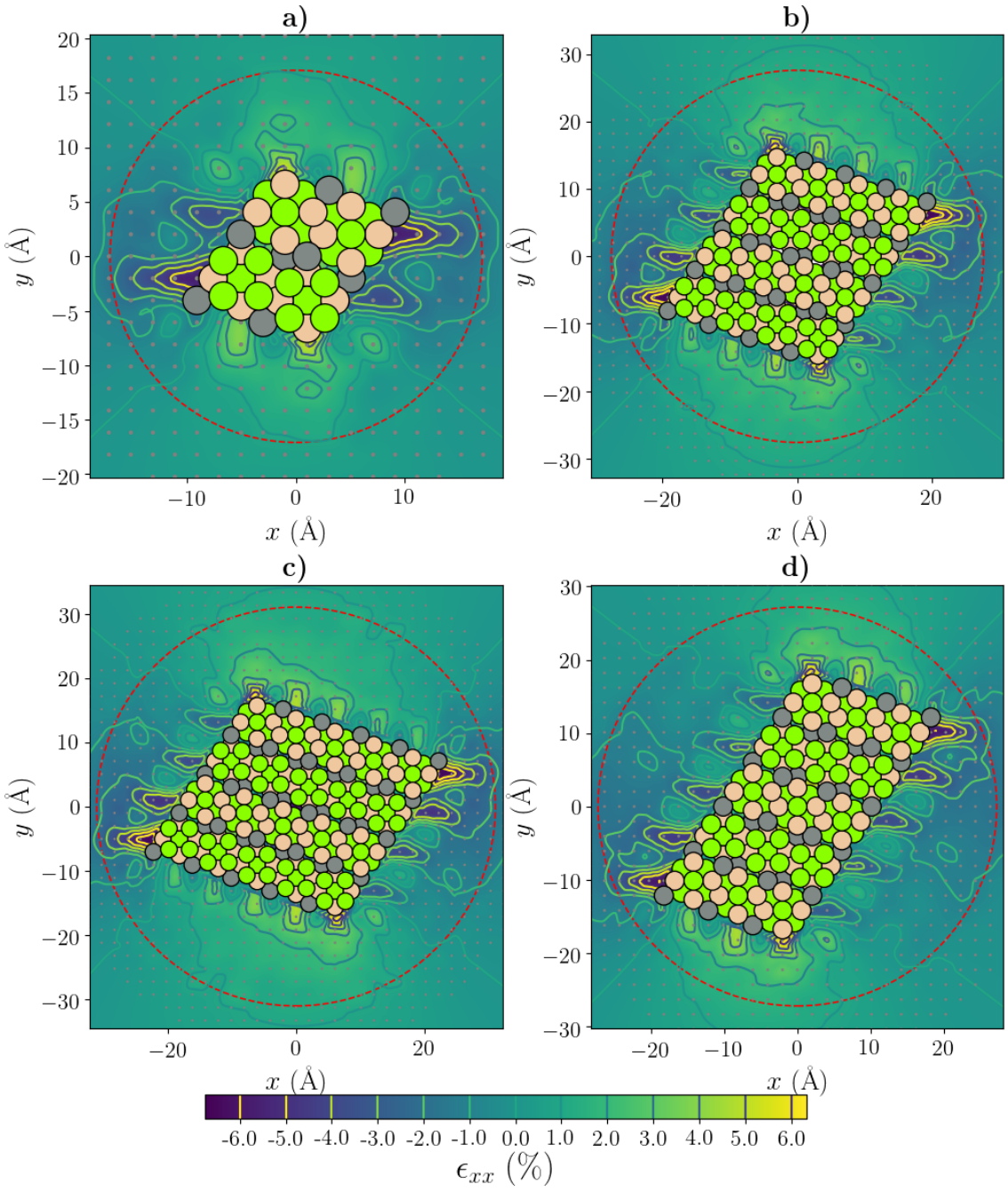

Figure 4.11: Contour plots by cubic interpolation of the strain component ϵ_{xx} for a **a)** 2×2, **b)** 4×4, **c)** 4×5, and **d)** 5×3 precipitate. The isolines indicate curves along which ϵ_{xx} is constant. The stippled, red line indicates the radius of the relaxable region. The grey dots indicate perfect aluminium lattice positions. The precipitate has been indicated.

Chapter 5

Concluding Remarks

The present work has presented a cluster-based modeling scheme for a semi-coherent precipitate in a surrounding host lattice based on electronic structure calculations by plane-wave DFT with static boundary conditions given by LET. A case-study was performed with the metastable hardening precipitate β″ from the industrially important Al-Mg-Si alloys. Convergence tests showed that the simulations were sufficiently converged with a static region width of $w = 7\,\text{Å}$ and a precipitate-static region distance of $\Delta = 6.57\,\text{Å}$. Atomic positions were converged to within approximately $0.01\,\text{Å}$ with a force criterion of $F_{\max} = 0.01\,\text{eV}\,\text{Å}^{-1}$ during structural relaxation.

Simulations with experimentally observed precipitate dimensions were performed. The calculated misfits m_a and m_c varied between 3.09%–4.25% and 4.32%–5.71% respectively and were between 10%–30% larger than corresponding experimental values in [9]. The values were in general smaller than reported bulk values, as β″ structure is constricted by the surrounding Al matrix. The misfit area A_{m} decreased with increasing precipitate size, and varied between 8.76%–9.75%, in relatively good agreement with the average of $A_{\text{m}} = 7.12\%$ from the experimental study [9]. The results show that the relaxed β″ structures are somewhat larger than previous experimental and theoretical counterparts, and are expected to be larger still if one uses a stricter force requirement on the structural relaxation.

The precipitates reduce their cross-sectional size in one lattice directions in response to increased size in the other direction. This has been attributed to the Poisson effect, and is in agreement with observation from previous experimental and theoretic studies of β″. The effect is visualized by fitting the misfit ratio to a

reciprocal expression $R_{\mathrm{m}} = C/R_{\mathrm{L}}$. The fitting seems to describe the data well, and the optimal coefficient was $C = 0.93$. In comparison, the experimental study [9] obtained $C = 1.00$.

The elastic strain in the aluminium matrix has been calculated. The strain along the [1 0 0] direction out from the surface Si atoms on the [2 3 0] interface showed a sharp change in derivative at the interface to the annulus. The data gives similar coefficients with [7] when fitting only the relaxable region data points with an exponential function. Finally, contour maps of strain around the different precipitate dimensions were presented. A comparison with previous works show they are very similar, except strain magnitude is generally higher along the precipitate-host matrix interface in the current work.

Bibliography

[1] B. Pedersen, "Aluminium," *Store norske leksikon*, Apr 2018. [Online]. Available: https://snl.no/aluminium [Accessed Jul. 10, 2018].

[2] F. Habashi, "Bayer's process for alumina production: A historical perspective," *Bulletin for the history of chemistry*, 1995. [Online]. Available: http://www.scs.illinois.edu/~mainzv/HIST/bulletin_open_access/num17-18/num17-18%20p15-19.pdf [Accessed Jul 10, 2018].

[3] The Aluminium Association. Aluminium alloys 101. [Online]. Available: http://www.aluminum.org/resources/industry-standards/aluminum-alloys-101 [Accessed Jul. 10, 2018].

[4] I. Ringdalen, S. Wenner, J. Friis, and J. Marian, "Dislocation dynamics study of precipitate hardening in Al-Mg-Si alloys with input from experimental characterization," *MRS Communications*, vol. 7, no. 3, p. 626633, 2017. [Online]. Available: https://doi.org/10.1557/mrc.2017.78

[5] H. S. Hasting *et al.*, "Composition of β″ precipitates in Al-Mg-Si alloys by atom probe tomography and first principles calculations," *Journal of Applied Physics*, vol. 106, no. 12, p. 123527, 2009. [Online]. Available: https://doi.org/10.1063/1.3269714

[6] F. J. H. Ehlers, S. Dumoulin, K. Marthinsen, and R. Holmestad, "Interface energy determination for the fully coherent β'' phase in Al-Mg-Si: making a case for a first principles based hybrid atomistic modelling scheme," *Modelling and Simulation in Materials Science and Engineering*, vol. 21, no. 8, p. 085018, 2013. [Online]. Available: http://stacks.iop.org/0965-0393/21/i=8/a=085018

[7] P. H. Ninive, O. M. Løvvik, and A. Strandlie, "Density functional study of the β'' phase in Al-Mg-Si alloys," *Metallurgical and Materials*

Transactions A, vol. 45, no. 6, pp. 2916–2924, Jun 2014. [Online]. Available: https://doi.org/10.1007/s11661-014-2214-4

[8] P. H. Ninive *et al.*, "Detailed atomistic insight into the β″ phase in Al-Mg-Si alloys," *Acta Materialia*, vol. 69, no. Supplement C, pp. 126 – 134, 2014. [Online]. Available: http://www.sciencedirect.com/science/article/pii/S1359645414000731

[9] S. Wenner and R. Holmestad, "Accurately measured precipitatematrix misfit in an Al-Mg-Si alloy by electron microscopy," *Scripta Materialia*, vol. 118, pp. 5 – 8, 2016. [Online]. Available: http://www.sciencedirect.com/science/article/pii/S1359646216300756

[10] D. Rodney, L. Ventelon, E. Clouet, L. Pizzagalli, and F. Willaime, "Ab initio modeling of dislocation core properties in metals and semiconductors," *Acta Materialia*, vol. 124, pp. 633 – 659, 2017. [Online]. Available: http://www.sciencedirect.com/science/article/pii/S1359645416307492

[11] P. H. Ninive, "Towards a complete description of aluminium from atomistic modeling. a parameter-free study of hardening precipitates in al alloys," Ph.D. dissertation, Gjøvik University College, Gjøvik, Norway, Dec. 2014. [Online]. Available: http://urn.nb.no/URN:NBN:no-52445

[12] Manny. (2017, Jul) All about brass. [Online]. Available: https://www.mkmjewelry.com/all-about-brass/ [Accessed Jun. 28, 2018].

[13] N. Christensen and A. Almar-Næss, "Stål," *Store norske leksikon*, May 2017. [Online]. Available: https://snl.no/st%C3%A5l [Accessed Jun 28, 2018].

[14] COMET METALS homepage. Aluminum alloy 1235. [Online]. Available: https://www.cometmetals.com/metal-detail?met_id=10767&product_txt=aluminum&pg_id=5141 [Accessed Jun. 28, 2018].

[15] ESAB KNOWLEDGE CENTER. Understanding the aluminum alloy designation system. [Online]. Available: https://www.esabna.com/us/en/education/blog/understanding-the-aluminum-alloy-designation-system.cfm [Accessed Jun. 28, 2018].

[16] J. D. Verhoeven, *Fundamentals of Physical Metallurgy*, 1st ed. New York, USA: John Wiley & Sons, 1975.

[17] P. Mukhopadhyay, "Alloy designation, processing, and use of AA6XXX series aluminium alloys," *ISRN Metallurgy*, vol. 2012, no. 165082, 2012. [Online]. Available: https://doi.org/10.5402/2012/165082

[18] M. Takeda, F. Ohkubo, T. Shirai, and K. Fukui, "Stability of metastable phases and microstructures in the ageing process of Al–Mg–Si ternary alloys," *Journal of Materials Science*, vol. 33, no. 9, pp. 2385–2390, May 1998. [Online]. Available: https://doi.org/10.1023/A:1004355824857

[19] A. G. Frøseth, R. Høier, P. M. Derlet, S. J. Andersen, and C. D. Marioara, "Bonding in MgSi and Al-Mg-Si compounds relevant to Al-Mg-Si alloys," *Phys. Rev. B*, vol. 67, p. 224106, Jun 2003. [Online]. Available: https://link.aps.org/doi/10.1103/PhysRevB.67.224106

[20] S. J. Andersen, H. W. Zandbergen, J. Jansen, C. Træholt, U. Tundal, and O. Reiso, "The crystal structure of the β'' phase in Al-Mg-Si alloys," *Acta Materialia*, vol. 46, no. 9, pp. 3283 – 3298, 1998. [Online]. Available: http://www.sciencedirect.com/science/article/pii/S135964549700493X

[21] J. H. Chen, E. Costan, M. A. van Huis, Q. Xu, and H. W. Zandbergen, "Atomic pillar-based nanoprecipitates strengthen AlMgSi alloys," *Science*, vol. 312, no. 5772, pp. 416–419, 2006. [Online]. Available: http://science.sciencemag.org/content/312/5772/416

[22] A. K. Giri and G. B. Mitra, "Extrapolated values of lattice constants of some cubic metals at absolute zero," *Journal of Physics D: Applied Physics*, vol. 18, no. 7, p. L75, 1985. [Online]. Available: http://stacks.iop.org/0022-3727/18/i=7/a=005

[23] W. P. Davey, "Precision measurements of the lattice constants of twelve common metals," *Phys. Rev.*, vol. 25, pp. 753–761, Jun 1925. [Online]. Available: https://link.aps.org/doi/10.1103/PhysRev.25.753

[24] S. Wenner, L. Jones, C. D. Marioara, and R. Holmestad, "Atomic-resolution chemical mapping of ordered precipitates in Al alloys using energy-dispersive

X-ray spectroscopy," *Micron*, vol. 96, no. Supplement C, pp. 103 – 111, 2017. [Online]. Available: http://www.sciencedirect.com/science/article/pii/S096843281730001X

[25] C. Wolverton and V. Ozoliņš, "Entropically favored ordering: The metallurgy of Al_2Cu revisited," *Phys. Rev. Lett.*, vol. 86, pp. 5518–5521, Jun 2001. [Online]. Available: https://link.aps.org/doi/10.1103/PhysRevLett.86.5518

[26] F. J. H. Ehlers and R. Holmestad, "Ab initio based interface modeling for fully coherent precipitates of arbitrary size in Al alloys," *Computational Materials Science*, vol. 72, no. Supplement C, pp. 146 – 157, 2013. [Online]. Available: http://www.sciencedirect.com/science/article/pii/S0927025613000517

[27] Y. Wang, Z.-K. Liu, L.-Q. Chen, and C. Wolverton, "First-principles calculations of $\beta''-Mg_5Si_6/\alpha-Al$ interfaces," *Acta Materialia*, vol. 55, no. 17, pp. 5934 – 5947, 2007. [Online]. Available: http://www.sciencedirect.com/science/article/pii/S1359645407004673

[28] A. Kelly and K. M. Knowles, *Crystallography and Crystal Defects*, 2nd ed. Chichester, United Kingdom: John Wiley & Sons, 2012.

[29] P. Hohenberg and W. Kohn, "Inhomogeneous electron gas," *Phys. Rev.*, vol. 136, pp. B864–B871, Nov 1964. [Online]. Available: https://link.aps.org/doi/10.1103/PhysRev.136.B864

[30] VASP homepage. What is VASP? [Online]. Available: https://www.vasp.at/index.php/about-vasp/59-about-vasp [Accessed Jul. 24, 2018].

[31] A. Eichler. (2003, Feb.) Sampling the brillouin zone. Universität Wien. Sensengasse 8, A-1090 Wien, Austria. [Online]. Available: https://www.vasp.at/vasp-workshop/slides/k-points.pdf [Accessed Jul. 9, 2018].

[32] D. S. Sholl and J. A. Steckel, *Density functional theory: a practical introduction*, 1st ed. New Jersey, USA: John Wiley & Sons, sep 2009.

[33] G. Kresse, M. Marsman, and J. Furthermüller, *VASP the GUIDE*, Computational Materials Physics, Faculty of Physics, Universität Wien, Sensengasse 8/12, A-1090 Wien, Austria, Apr. 2016. [Online]. Available: https://cms.mpi.univie.ac.at/vasp/vasp.pdf [Accessed Jul. 9, 2018].

[34] R. M. Wentzcovitch, J. L. Martins, and P. B. Allen, "Energy versus free-energy conservation in first principles molecular dynamics," *Phys. Rev. B*, vol. 45, pp. 11 372–11 374, May 1992. [Online]. Available: https://link.aps.org/doi/10.1103/PhysRevB.45.11372

[35] M. Weinert and J. W. Davenport, "Fractional occupations and density-functional energies and forces," *Phys. Rev. B*, vol. 45, pp. 13 709–13 712, Jun 1992. [Online]. Available: https://link.aps.org/doi/10.1103/PhysRevB.45.13709

[36] J. D. Eshelby, "The determination of the elastic field of an ellipsoidal inclusion, and related problems," *Proceedings of the Royal Society of London A: Mathematical, Physical and Engineering Sciences*, vol. 241, no. 1226, pp. 376–396, 1957. [Online]. Available: http://rspa.royalsocietypublishing.org/content/241/1226/376

[37] P. Alfeld, "A trivariate clough–tocher scheme for tetrahedral data," *Computer Aided Geometric Design*, vol. 1, no. 2, pp. 169 – 181, 1984. [Online]. Available: http://www.sciencedirect.com/science/article/pii/0167839684900293

[38] *scipy.interpolate.griddata*, The SciPy community. [Online]. Available: https://docs.scipy.org/doc/scipy/reference/generated/scipy.interpolate.griddata.html [Accessed Jun. 29, 2018].

[39] C. Ravi and C. Wolverton, "First-principles study of crystal structure and stability of Al-Mg-Si-(Cu) precipitates," *Acta Materialia*, vol. 52, no. 14, pp. 4213 – 4227, 2004. [Online]. Available: http://www.sciencedirect.com/science/article/pii/S1359645404003106

[40] D. Giofré, T. Junge, W. A. Curtin, and M. Ceriotti, "Ab initio modelling of the early stages of precipitation in Al-6000 alloys," *Acta Materialia*, vol. 140, pp. 240 – 249, 2017. [Online]. Available: http://www.sciencedirect.com/science/article/pii/S1359645417306614

[41] F. J. H. Ehlers, S. Dumoulin, and R. Holmestad, "3D modelling of β'' in Al-Mg-Si: Towards an atomistic level ab initio based examination of a full precipitate enclosed in a host lattice," *Computational*

Materials Science, vol. 91, pp. 200 – 210, 2014. [Online]. Available: http://www.sciencedirect.com/science/article/pii/S0927025614003024

[42] V. Vitek, "Structure of dislocation cores in metallic materials and its impact on their plastic behaviour," *Progress in Materials Science*, vol. 36, pp. 1 – 27, 1992. [Online]. Available: http://www.sciencedirect.com/science/article/pii/007964259290003P

[43] V. B. Shenoy and R. Phillips, "Finite-sized atomistic simulations of screw dislocations," *Philosophical Magazine A*, vol. 76, no. 2, pp. 367–385, 1997. [Online]. Available: https://doi.org/10.1080/01418619708209981

[44] S. Ofstad, "First principles study of the displacement field surrounding β″ in aluminium," Student project, Norwegian University of Science and Technology, Trondheim, Norway, 2017.

[45] P. E. Blöchl, "Projector augmented-wave method," *Phys. Rev. B*, vol. 50, pp. 17 953–17 979, Dec 1994. [Online]. Available: https://link.aps.org/doi/10.1103/PhysRevB.50.17953

[46] G. Kresse and D. Joubert, "From ultrasoft pseudopotentials to the projector augmented-wave method," *Phys. Rev. B*, vol. 59, pp. 1758–1775, Jan 1999. [Online]. Available: https://link.aps.org/doi/10.1103/PhysRevB.59.1758

[47] M. Methfessel and A. T. Paxton, "High-precision sampling for Brillouin-zone integration in metals," *Phys. Rev. B*, vol. 40, pp. 3616–3621, Aug 1989. [Online]. Available: https://link.aps.org/doi/10.1103/PhysRevB.40.3616

[48] Livermore Software Technology Corporation. Ls-dyna. [Online]. Available: http://www.lstc.com/products/ls-dyna [Accessed Jun. 29, 2018].

[49] F. J. Ehlers, S. Dumoulin, K. Marthinsen, and R. Holmestad, "Interfacial and strain energy analysis from ab initio based hierarchical multi-scale modelling: The Al-Mg-Si alloy β" phase," vol. 794, pp. 640–645, 7 2014. [Online]. Available: https://doi.org/10.4028/www.scientific.net/MSF.794-796.640

Appendices

Appendix A

Input files for VASP

VASP requires four input files to run.

- INCAR determines the general behavior of the VASP code by a list of keywords which define simulation parameters.
- KPOINTS defines the k-points used for sampling of the reciprocal space.
- POSCAR gives the atomic positions and the size of the simulation supercell.
- POTCAR defines the projector augmented-wave potentials used.

Examples of INCAR and KPOINTS files used for simulations in the present work follow.

A.1 INCAR file

```
INCAR for ionic relaxation,

! Electronic relaxation
ALGO   = Fast
NELMIN = 4          ! Minimum # of electronic steps
EDIFF  = 1e-05
ENCUT  = 400        ! Cut-off energy for plane wave expansion
PREC   = Accurate   ! Normal/Accurate
LREAL  = Auto       ! Projection in reciprocal space?
```

```
ISMEAR = 1          ! 1 gives Methfessel-Paxton method. -5 does not
    work for large super cells because the number of kpoints is less
    than 3
SIGMA  = 0.2        ! Smearing width
ISPIN  = 1          ! Spin polarization?
AMIN   = 0.01       ! Charge mixing. Changed to 0.01 on recommendation
    from slurm file because large supercell

! Ionic relaxation
EDIFFG = -0.01
NSW    = 80         ! Max # of ionic steps
MAXMIX = 80         ! Keep dielectric function between ionic movements
IBRION = 1          ! Using Conjugate gradient method. Algorithm for
    ions. 0: MD 1: QN/DIIS 2: CG
ISIF   = 2          ! Relaxation. 2: ions 3: ions+cell
! ADDGRID= .TRUE.     ! More accurate forces with PAW
POTIM = 0.6
! Output options
NWRITE = 1          ! Write electronic convergence at first step only

! Memory handling
NPAR   = 8           !sqrt(CPUs)
LPLANE  = .TRUE.
LSCALU  = .FALSE
NSIM   = 4
LWAVE = .True.
```

A.2 KPOINTS file

```
Max k-point distance: 0.180000
0
Gamma
 1 1 9
 0  0  0
```